

**Master Thesis**

**Studies on homologous flares at quadrupole  
magnetic field using force-free field modeling**

**Yusuke Kawabata**

**Department of Earth and Planetary Science  
Graduate School of Science, The University of Tokyo**

**February 29, 2016**



# Abstract

Solar flares are known as abrupt energy release events by magnetic reconnection. The standard 2D model of solar flares, which is called CSHKP model, explains large eruptive flares well. We analyzed three M-class flares occurring on 2 February 2014, which are difficult to understand with the CSHKP model. Our investigations primarily focused on the 3D coronal magnetic field structures formed in the flaring region for attempting to understand why three similar flares (labeled flare 1, flare 2, and flare 3, respectively) are successively produced in the region.

Four flare ribbons were observed at the footpoints of three flaring structures by Atmospheric Imaging Assembly aboard the *Solar Dynamics Observatory*. The observed flare ribbons and coronal flaring structures show similarity in the three flares, which are called homologous flares. The flare ribbons were located in the four magnetic regions (P1, P2, N1, and N2) at the solar surface. We derived the three dimensional magnetic field configuration using force-free field modeling with *Hinode*/Spectropolarimeter data. We used the squashing factor defined by Titov (1999) to identify the location of quasi-separatrix layers, i.e., QSLs.

The magnetic field lines from the force-free field modeling give fairly good correspondences among many bright flare kernels in the flare ribbons, although we still need to improve the modeling fidelity. The magnetic field lines rooted on the flare ribbons forms the three-dimensional quadrupole magnetic configuration with an X-shape separatrix structure in the upper atmosphere. The region of the highest squashing factor is located at the height of 2000~3000km from the photosphere, suggesting that the magnetic reconnection

may take place at the lower atmosphere. The magnetic flux in the N1 sunspot appears to be highly twisted, because the QSLs structure derived with the assumption of the potential field is completely different from what obtained with 3D magnetic field configuration from the NLFFF modeling. The QSLs structure derived with the NLFFF results for the SP data taken one day before the occurrence of flare 1 is different from that derived with the data taken one hour before flare 1. This indicates that the QSLs structure was formed during the day due to the emergence or the transverse photospheric motions of the magnetic flux in N1. The temporal evolution of magnetic flux suggests that both the existence of emerging activities and the converging motions in and around the N1 sunspot region. Focused on homology and differences in the flares, although the spatial distribution of the flare ribbons is similar to each other in the main period of the flares, there is a little difference in the temporal evolution of X-ray flux. Such a difference might attribute to the difference in triggering the onset of these flares. Flare 1 occurred after the occurrence of another flare event at the east side of the flare 1 region, while flare 2 occurred after the upward motion of a dark material. This may indicate that the magnetic field shows a similar topology, but the trigger mechanism can alter the temporal behaviors of the energy release.

# 要旨

太陽フレアは、磁気リコネクションによりコロナ磁場に蓄積された磁気エネルギーが突発的に解放される現象として知られる。太陽フレアには「標準モデル」と呼ばれる CSHKP モデルが存在し、フィラメント放出を伴う eruptive なツーリボンフレアを良く説明する。本研究では CSHKP モデルでは解釈が難しい、4 つの磁極上でフレアリボンが観測されたホモロガスフレアの複雑な 3 次元磁場構造を調べることを目的とした。解析した領域は 2014 年 2 月 2 日に 3 回の M クラスフレアを起こした NOAA AR 11967 である。本研究ではそれぞれフレア 1、フレア 2、フレア 3 と名付けた。太陽観測衛星「Solar Dynamics Observatory」に搭載された Atmospheric Imaging Assembly によりそれぞれのフレアにおいて 4 つのフレアリボンと 3 つのポストフレアループが観測された。3 つのフレアにおいてこれらのフレアリボンとポストフレアループの形状は酷似しており、ホモロガスフレアと称されるイベントであることが示された。

フレアリボンが現れた 4 つの磁極 (P1、P2、N1、N2) 付近の磁場構造に着目し、非線形フォースフリー磁場モデリングによって 3 次元磁場構造を調べた。また得られた 3 次元磁場を用いて Titov (1999) で Quasi-separatrix layers (QSLs) の指標として定義された squashing factor を計算した。

フォースフリー磁場モデリングにより導出された磁力線の両端の足元は観測されたフレアリボンのカーネルと非常に良く一致したが、観測と一致しない磁場構造も確認され、モデリングの改善の必要性がある。磁気リコネクションが起きたと推定される squashing factor が最も高い領域は光球から 2000~3000km に位置し、比較的低い大気において磁気リコネクションが起こったことが示唆された。フレア 1 の

1 日前において N1 の領域でフレア直前の QSLs とは異なる構造を持っており、このことはフレア直前の N1 における QSLs が 1 日間の間で形成されたことを示唆している。そこで 2014 年 2 月 1 日から 2 月 2 日までの垂直磁場フラックスを測定したところ、N1 の領域で継続的にフラックス増加の傾向が見られた。この浮上磁場もしくは光球磁場フラックスの水平移動がフレアのエネルギー蓄積に貢献していることが推測される。また 3 つのフレアに関して、フレアリボンは非常に類似した形状が観測されたが、X 線フラックスの時間発展は異なる振る舞いを見せた。観測からその違いはフレアの前兆現象に原因がある可能性が示唆された。フレア 1 が起こる前にはフレア 1 の領域の東側でもう一つのフレアイベントが観測されており、フレア 2 の 30 分前には暗い物質の上昇する動きが観測されている。このことはフレアの前兆現象がエネルギー解放の振る舞いを変える可能性があることを示唆する。

# Contents

<b>Abstract</b>	<b>i</b>
<b>要旨</b>	<b>iii</b>
<b>1 General Introduction</b>	<b>1</b>
1.1 Present understanding of solar flares . . . . .	1
1.1.1 CSHKP model . . . . .	1
1.1.2 Energy storage, trigger, and 3D magnetic configuration . . . . .	2
1.2 Homologous flares . . . . .	7
1.3 Magnetic reconnection . . . . .	7
1.3.1 Magnetic reconnection (2D) . . . . .	8
1.3.2 Magnetic reconnection (3D) . . . . .	10
1.4 Force-free field . . . . .	11
1.4.1 Potential field . . . . .	13
1.4.2 Nonlinear force-free field . . . . .	13
1.5 Purpose of this thesis . . . . .	14
<b>2 Observations</b>	<b>16</b>
2.1 <i>Hinode</i> SOT Observations . . . . .	16
2.2 <i>SDO</i> Observations . . . . .	19
<b>3 Analysis Methods</b>	<b>22</b>
3.1 Observational data processing . . . . .	22

3.2	Force-free field modeling . . . . .	24
3.3	Squashing factor . . . . .	27
<b>4</b>	<b>Results</b>	<b>31</b>
4.1	Properties of the flares from observations . . . . .	31
4.1.1	Flare ribbons, post flare loops, and photospheric magnetic fields .	31
4.1.2	Preflare activities . . . . .	42
4.2	3D magnetic field structure in the corona . . . . .	45
4.2.1	Distribution of magnetic field lines in the flaring region . . . . .	45
4.2.2	Comparisons with observations . . . . .	47
4.3	Quasi-Separatrix Layers . . . . .	50
4.3.1	Spatial distribution of the QSLs . . . . .	50
4.3.2	Formation of the non-potential structure . . . . .	55
<b>5</b>	<b>Discussion</b>	<b>57</b>
5.1	Validity of the NLFFF modeling . . . . .	57
5.2	Energy release site and energy storage . . . . .	59
5.3	Homology and differences in the flares . . . . .	61
5.4	Comparison with the previous studies and outlooks . . . . .	62
<b>6</b>	<b>Summary and Future Works</b>	<b>65</b>
	<b>Acknowledgments</b>	<b>70</b>
	<b>References</b>	<b>72</b>

# Chapter 1

## General Introduction

Solar flares are explosive energy release events in the solar atmosphere. When solar flares occur, electromagnetic radiation is emitted in the broad spectrum range from radio to  $\gamma$ -rays. Solar flares are often accompanied by coronal mass ejections (CME) which disturb Earth's magnetosphere and lead to geomagnetic storms. The total energy released by a solar flare is  $10^{29} \sim 10^{32}$  ergs. The energy source is thought to be magnetic energy generated by the convection at the solar surface (photosphere) and stored in the upper atmosphere (chromosphere and corona). Magnetic reconnection is believed to play an important role in converting the magnetic energy to kinetic and thermal energies in the solar atmosphere. In this chapter, we introduce observational and theoretical aspects of solar flares and the motivation of our study.

### 1.1 Present understanding of solar flares

#### 1.1.1 CSHKP model

Solar flares have been observed and studied for a long time (see e.g. Janvier et al. (2015)). Many observed flares are frequently discussed with the standard 2D flare model, which is called the CSHKP model constructed by Carmichael (1964), Sturrock (1966), Hirayama (1974), and Kopp & Pneuman (1976). This model explains some features of solar flares

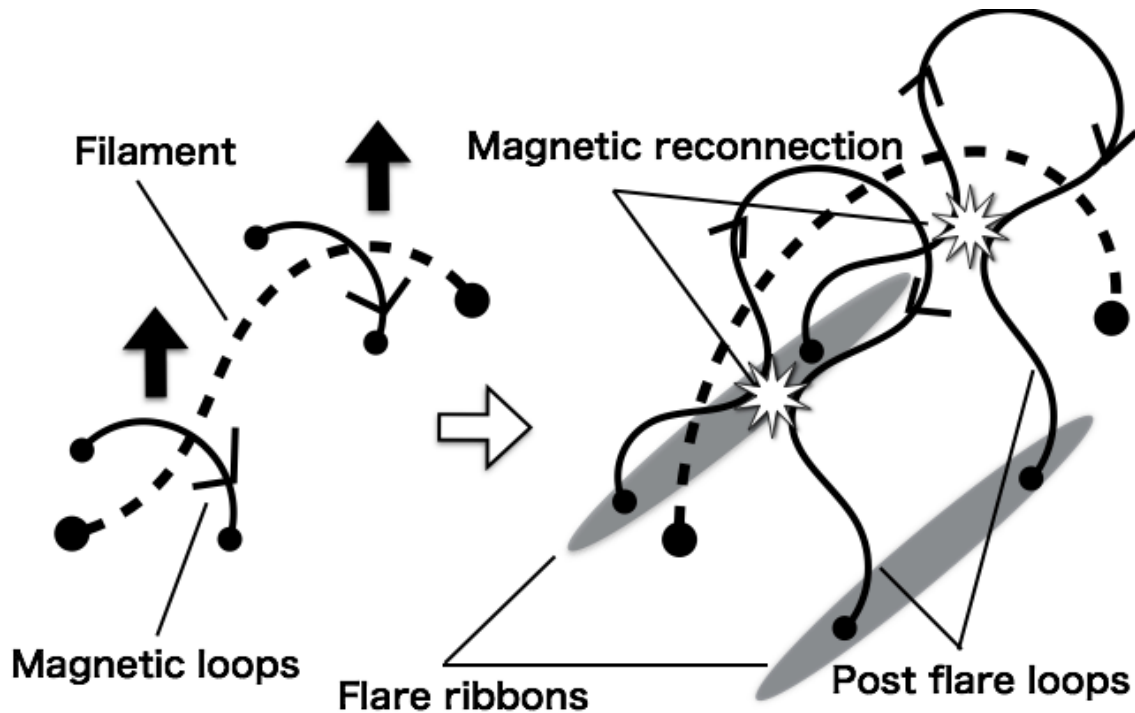


Figure 1.1: The sketch of CSHKP model. Rising of an destabilized filament creates the anti-parallel magnetic field below the filament, where magnetic reconnection take places.

shown in Figure 1.1, which is described in 3D for easy comparison with observed features in Figure 1.2. Rising of a filament with MHD instability results in expanding overlying magnetic loops and magnetic reconnection is induced in the solar corona. Hot plasmas and accelerated particles are generated by magnetic reconnection. The thermal conduction from the hot plasma and impingement of accelerated particles gives the heat to the chromosphere, which form chromospheric flare ribbons as shown in Figure 1.2. The transient heat inputs to the flare ribbons cause so-called chromospheric evaporation and fill the flare loops with dense heated plasmas (Figure 1.2).

### 1.1.2 Energy storage, trigger, and 3D magnetic configuration

The CSHKP model answers the mechanism of energy release and captures the observational properties of many flares. However, there are several unsolved issues. One issue is how the magnetic energy for solar flares is stored in the solar atmosphere. Second, what mechanism triggers solar flares? Third, how many kinds of magnetic configuration

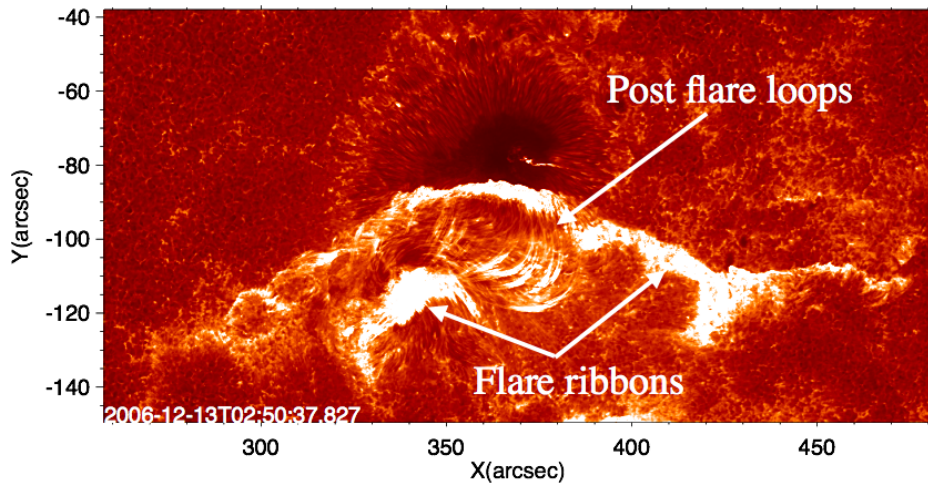


Figure 1.2: An image of Ca H II line observed by SOT/*Hinode*. We can see flare ribbons structure clearly. There also can be seen arcade post flare loop structure.

exist for producing flares and how are they formed? Since only bipolar field is considered in the CSHKP model which includes a limited number of observed flares, we need to investigate flares occurring with other magnetic field configuration, such as multipolar magnetic fields.

The energy released by solar flares is stored as magnetic energy in the solar atmosphere. The lowest state of the magnetic field configuration is called the potential (current-free) field (detailed description will be shown in chapter 3). When the magnetic field is deviated from the potential field, the field has the excess energy (called free energy), which can be used for energy release in solar flares. The free energy is stored as electric currents in non-potential field, and therefore the question becomes how the magnetic field configuration possessing high current density can be created. There are two candidates for the energy storage in the coronal magnetic fields: twisted flux emergence and transverse photospheric motion. Numerical simulations suggest that it is necessary for a flux rope to be highly twisted in order to continue to rise through the convection zone (Emonet & Moreno-Insertis, 1998). Observations also show that flux tubes are twisted when they emerge (Leka et al., 1996). Current carrying flux tubes inject free energy to the system. On the other hand, the transverse photospheric motions such as twisting and shearing mo-

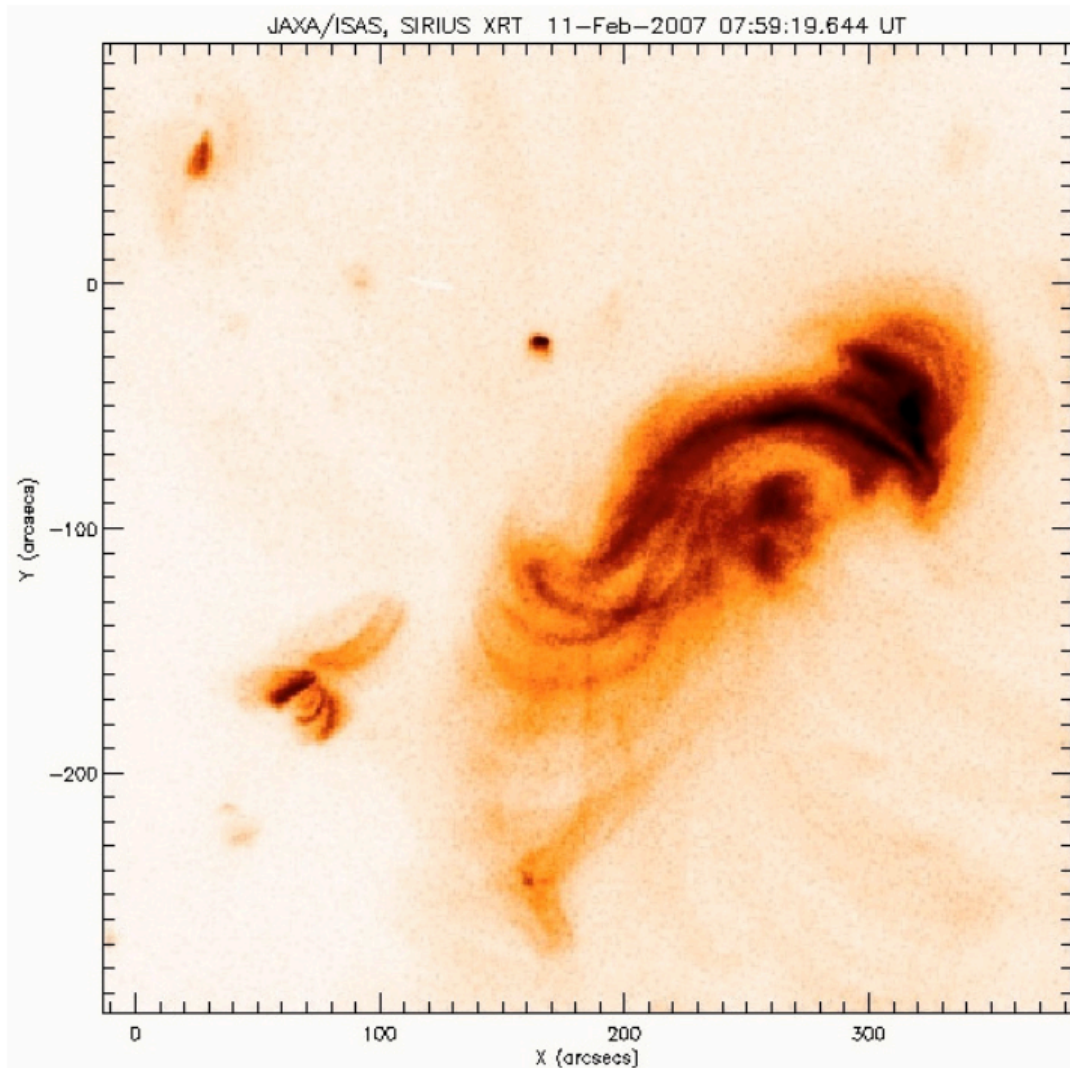


Figure 1.3: The sigmoid image observed by X-ray Telescope (XRT) on board the *Hinode*. This figure comes from Figure 2 of McKenzie & Canfield (2008)

tions can also produce free energy in the magnetic field structure. The sheared loops are often observed as J- or S- shaped sigmoids in soft X-rays (SXR) before flare occurs (see Figure 1.3 from McKenzie & Canfield (2008)). Rotating motions of the sunspots may be observed before flares (Louis et al., 2014) and play an important role in storing free energy.

The trigger mechanism of solar flares is now getting more attention. With regard to flares accompanied by CME, in other words eruptive flares, there are many kinds of models summarized in Aulanier (2014). In terms of three-dimensional magnetohydro-

dynamics (MHD) simulations, they concluded that only two distinct models can initiate eruptive flares: the magnetic breakout and the torus instability. The both models have the same concept; it is necessary for the filament eruption that the magnetic pressure overcomes the magnetic tension from the overlying loop. The magnetic breakout model was proposed by Antiochos et al. (1999). The concept of their model is lowering the magnetic tension from overlying magnetic loops by magnetic reconnection occurring at high altitude in the multipolar field. Observational evidence of the magnetic breakout model was reported by Aulanier et al. (2000). They showed the existence of the magnetic null point above a sheared magnetic field by magnetic field extrapolation and the evidence of reconnection at the null point before the flare by comparing between flare ribbons and footpoint of the magnetic field lines. The torus instability is the ideal loss of equilibrium of a flux rope, first proposed by Bateman (1978) in tokamaks and applied to solar physics by Kliem & Török (2006). From their theoretical model, the filament eruption can occur when the filament reached at a critical height where the magnetic tension from overlying loops decreases faster than the magnetic pressure from the filament. The torus instability causes filament eruption in 3D MHD simulations (Aulanier et al., 2010). In the case of confined flares, which do not produce CME, the emerging flux is thought to be the main trigger of solar flares (Heyvaerts et al., 1977; Forbes & Priest, 1984). A flux tube emerging from the subphotosphere forms the current density layer with the preexisting field lines and when the currents reach a critical value, the energy release by magnetic reconnection occurs. The flux tube emergence is also important in eruptive flares (Chen & Shibata, 2000; Kusano et al., 2012), which may cause a loss of equilibrium.

While the CSHKP model describes many observed behaviors of some solar flares very well, there are many flares difficult to understand with the CSHKP model, which is mainly caused by complex three-dimensional magnetic field structure. Liu et al. (2014) reported an unorthodox flare whose temperature structure is different from that predicted by the CSHKP model. As shown by Tsuneta (1996), the outer part of the SXR flare structure have higher temperature than inner portion, which is well explained by the CSHKP

model; the outer part is heated by slow MHD standing shocks formed above the flare structure. The flare analyzed by Liu et al. (2014) displays an inverse temperature structure (The outer portion has lower temperature). They performed nonlinear force-free field (NLFFF) modeling and investigated coronal 3D magnetic structure around the flaring region. Note that the details of NLFFF modeling will be described in section 1.4. They concluded that there are multiple energy release sites that produce the unorthodox temperature structure. Dalmasse et al. (2015) also analyzed a nontypical flare. In this flare loops were formed above the filament and the filament did not erupt. They also investigated 3D magnetic structure using linear force-free field modeling. They showed there were multiple reconnection sites and the filament did not play an important role in the flare.

In order to understand flares occurring at complex magnetic structures, we have to know where the magnetic reconnection might take place in three-dimensional magnetic structures. Since the main energy release and pre-flare activities occur in the upper atmosphere, i.e., chromosphere and corona, it is important to understand the magnetic field configuration in the upper atmosphere. Although we can obtain the photospheric magnetic fields by polarimetric observations, it is difficult to obtain magnetic fields in the chromosphere and the corona because the signal of the polarization is extremely low. Therefore, in addition to morphology of soft X-ray and EUV corona, NLFFF modeling is recently used instead when discussing 3D magnetic fields in the corona. However, one of the assumptions in NLFFF modeling (the magnetic pressure greatly surpasses the gas pressure) is not achieved near the photosphere. Currently, observations for diagnosing magnetic field in the chromosphere are under development with the ground-based telescopes, which will be extended to space borne observations, such as *Solar-C* in the future. It is important to evaluate the validity of the present NLFFF modeling and prepare the modeling including chromospheric magnetic field for the future observation.

## 1.2 Homologous flares

Some solar flares may recur at the same locations in the same active region and they show similar shapes of flare ribbons and post flare loops in the X-ray and EUV observations. Such flares are called homologous flares (Gaizauskas & Svestka, 1987). The time interval of their repetition is known from a few hours to several days and there is no consistent relationship between repetition interval and the magnitude of X-ray intensity (Martres et al., 1984; Gaizauskas, 1982).

Why can flares occur repeatedly? It is because not all free energy was used in the previous flare or there is continuous supply of the free energy to the location of homologous flares. Chandra et al. (2011) studied homologous flares and showed a continuous shearing motion by the rotating bipole in the flaring region. This result supports the continuous injection of free energy to the flaring region. Panesar et al. (2015) reported the subsequent eruption of the prominence leading to the removal of magnetic field above the active region and resulting in an eruptive flare.

Although Morita et al. (2001) and Chandra et al. (2011) investigated three-dimensional magnetic field structure (The former made use of the information obtained from the three different lines of sight and the latter performed the LFFF), there were few studies investigating 3D structures causing homologous flares. In addition, while investigating the cause of homologous flares is also an important topic, it may be useful to use such flares for identifying the energy storage and trigger of flares. We can isolate the energy storage and trigger mechanism of each homologous flare, since they have a similar three dimensional magnetic field structure.

## 1.3 Magnetic reconnection

As described above, magnetic reconnection is the central physical mechanism in converting the magnetic energy to thermal and kinetic energies in solar flares. In this section, we

will introduce works of 2D magnetic reconnection and move to the recent studies of 3D magnetic reconnection.

### 1.3.1 Magnetic reconnection (2D)

The word "magnetic reconnection" was first proposed by Dungey (1953) to explain particle acceleration in the magnetosphere. After that, Sweet (1958) proposed a reconnection model that considered the plasma flow in order to rapid energy release in solar flares. Parker (1963) estimated the time scale of energy release in the model of Sweet (1958) and showed that his model is not rapid enough for explaining the time scale of solar flares. The model is now called Sweet-Parker model, which is shown in the left panel of Figure 1.4 . The reconnection rate defined as  $M_A \equiv V_{\text{in}}/V_A$  of their model is,

$$M_A \sim \frac{1}{\sqrt{S}}, \quad (1.1)$$

where  $V_{\text{in}}$  is the velocity of the reconnection inflow,  $V_A$  is the Alfvén velocity, and  $S$  is the magnetic Reynolds number defined as,

$$S \equiv \frac{V_A L}{\eta}, \quad (1.2)$$

where  $L$  is a length of the current sheet and  $\eta$  is the magnetic diffusivity. In order to solve low reconnection rate of Sweet-Parker model, Petschek (1964) introduced slow-mode MHD shocks to his reconnection model, which is now called Petschek model and the field configuration is shown in the right panel of Figure 1.4. The reconnection rate in his model is,

$$M_A \leq \frac{\pi}{8 \ln(8S)}. \quad (1.3)$$

His model explained the time scale of solar flares ( $\sim 10^2 \text{sec}$ ).

With soft X-ray observations from *Yohkoh*, Nagashima & Yokoyama (2006) measured physical parameters of flares statistically and derived the reconnection rate in order of

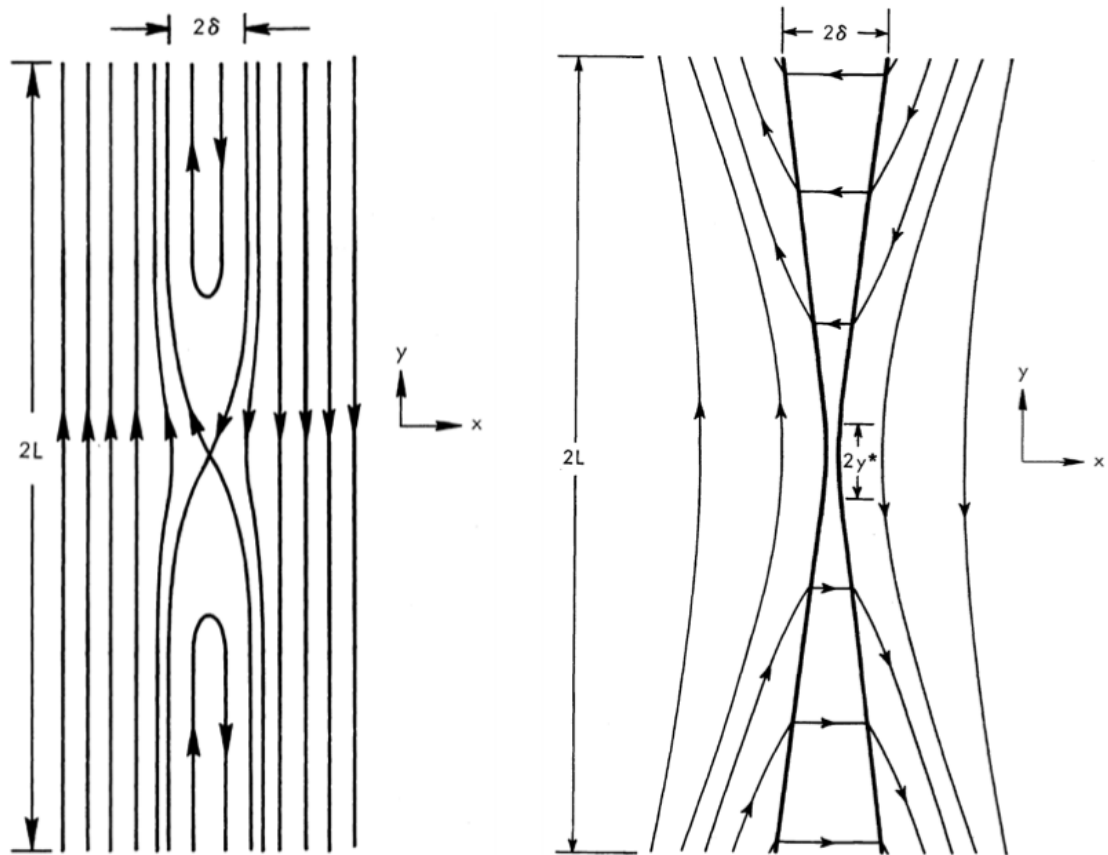


Figure 1.4: The magnetic reconnection model proposed by Sweet (1958) (left panel) and Petschek (1964) (right panel). Both figures are from Petschek (1964)

$10^{-3}$  to  $10^{-2}$ , matched with that of Petschek model within one order of magnitude, but the dependence on the magnetic Reynolds number is stronger than the Petschek model (eqn. (1.3)). With a spectroscopic observation, Hara et al. (2011) estimated the reconnection rate  $0.05 - 0.1$ , which is consistent with the Petschek model. They also presented a piece of evidence for the presence of the slow-mode and fast-mode MHD shocks from the observation.

### 1.3.2 Magnetic reconnection (3D)

The magnetic reconnection in 3D is completely different from in 2D. In 3D, magnetic reconnection can occur either at null points or in the absence of null points (Schindler et al., 1988). A necessary and sufficient condition for reconnection in 3D is the existence of the region where the ideal MHD breaks down,

$$\int \mathbf{E}_{\parallel} ds = 0, \quad (1.4)$$

where  $\mathbf{E}_{\parallel}$  is the component of the electric field parallel to the magnetic field line.

Priest & Démoulin (1995) proposed a model of reconnection in absence of null points. They suggested that reconnection in 3D occurs in quasi-separatrix layers (QSLs), where the gradient of field line linkage is steep but continuous. The quantitative definition of QSLs will be described in chapter 3. They considered the steady kinematic model in the three-dimensional sheared X field. They demonstrated that if the continuous flow is prescribed at the one footpoint of the field line, the resulting flow of the other footpoint can exceed the Alfvén speed in this ideal limit. If there is a diffusion region, the field lines are unfrozen and flip rapidly through the plasma. Although this study treats ideal and steady kinematic reconnection, the field line slipping is identified both in resistive 3D MHD simulations (Aulanier et al., 2010; Janvier et al., 2013) and X-ray and EUV observations (Aulanier et al., 2007; Dudík et al., 2014). The important suggestion in Priest & Démoulin (1995) is that magnetic reconnection in 3D can occur at QSLs and the

methods of defining QSLs were developed by later works (Demoulin et al., 1996; Titov, 1999; Titov et al., 2002; Titov, 2007; Pariat & Démoulin, 2012).

## 1.4 Force-free field

From polarimetric observations, we can obtain full Stokes vector and derive vector magnetic field in the photosphere with some assumptions. The energy release sites of solar flares mainly exist in the chromosphere and the corona, where it is challenging to measure the magnetic field because of low signal of polarization. Thus, force-free field modeling is currently a strong tool for getting insights of the magnetic structure in the corona in addition to morphological information of the coronal magnetic structures from EUV and soft X-ray imaging observations. The main concept of the force-free field modeling is the extrapolation of the coronal magnetic field from the spatial map of the magnetic field at the photosphere (Wiegmann & Sakurai, 2012). In the solar corona, the magnetic pressure dominates, so the plasma  $\beta (= 2\mu p/B^2)$ , which is the ratio between the plasma pressure and the magnetic pressure, is thought to be sufficiently small ( $\beta \ll 1$ ), as shown in Figure 1.5 (Gary, 2001), where  $\mu$  is the magnetic permeability. In such circumstance, the gas pressure can be neglected and the equilibrium is achieved when the Lorentz force vanishes, i.e., the magnetic tension and the magnetic pressure are balanced. That is,

$$\mathbf{j} \times \mathbf{B} = 0, \quad (1.5)$$

where  $\mathbf{j}$  is the current density, and the current density follows the Ampère's law

$$\nabla \times \mathbf{B} = \mu \mathbf{j}. \quad (1.6)$$

Equation (1.5) then can be written

$$\nabla \times \mathbf{B} = \alpha(\mathbf{r})\mathbf{B}, \quad (1.7)$$

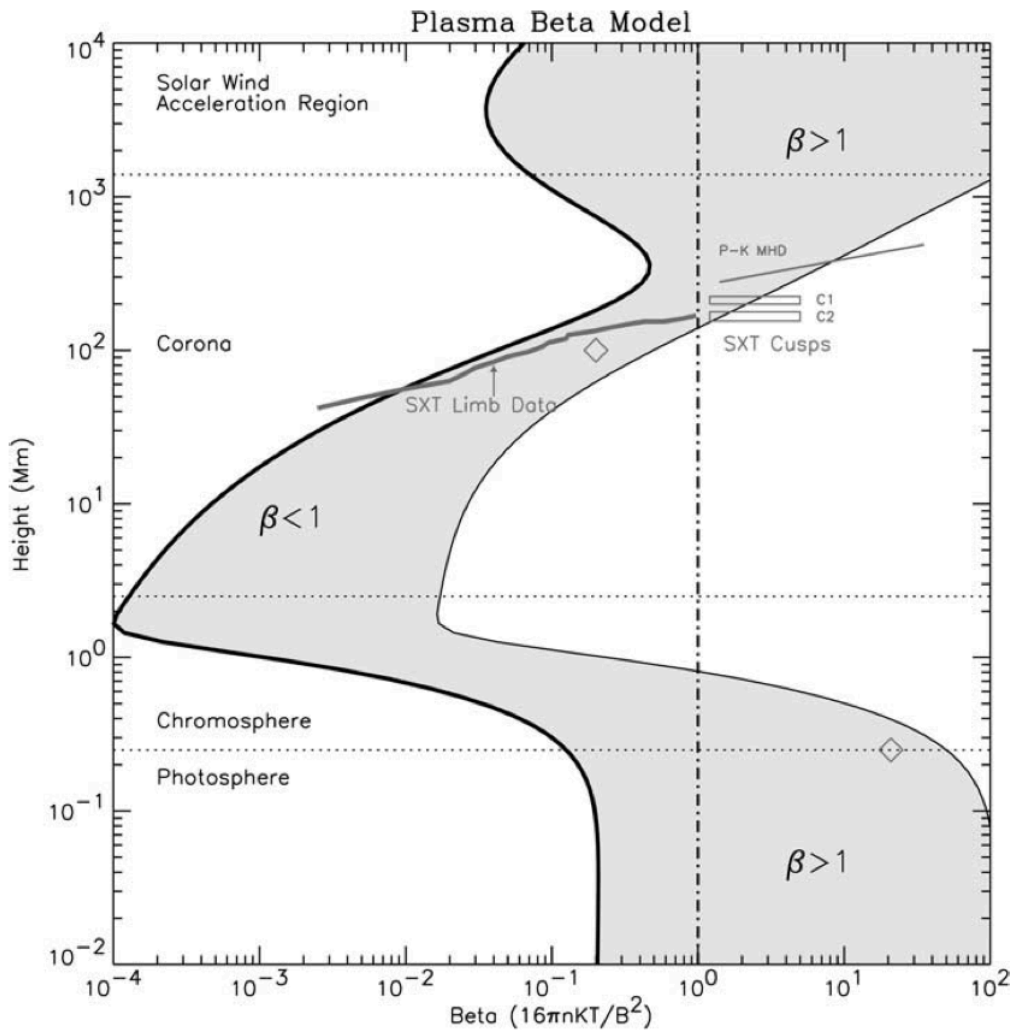


Figure 1.5: Variation of plasma  $\beta$  with height (Gary, 2001). While in the photosphere plasma  $\beta$  is more than unity, it becomes sufficiently small ( $\ll 1$ ) in the corona. The heavy line and the thin line correspond to the sunspot of 2500 G and the plage region of 150 G.

where  $\alpha$  is called the force-free parameter which has a spatial dependence and is constant along the field line. Since equation (1.7) is nonlinear, numerical methods are required to solve it.

### 1.4.1 Potential field

The most simple approximation of the force free field is called potential field (or current-free field  $j = 0$ ). Equation (1.7) reduces the Laplace equation

$$\nabla^2\Psi = 0, \quad (1.8)$$

where  $\Psi$  is the scalar magnetic potential, and there is an analytic solution (Priest, 2014)

$$\Psi = a \exp(ik_x x + ik_y y - kz), \quad (1.9)$$

where  $k_x$  and  $k_y$  are wave number of each component and  $k^2 = k_x^2 + k_y^2$ .

There are several methods to find potential fields. One of the methods is called Green's function method (Schmidt, 1964). In this method, from analogy of the electric field, a series of monopoles at  $(x', y', 0)$  are considered and the scalar potential can be written,

$$\Psi(x, y, z) = \int B_n(x', y') G_n(x, y, z, x', y') dx' dy', \quad (1.10)$$

where  $B_n$  is the magnetic field normal to the bottom boundary and  $G_n$  is the Green's function. If the  $B_n$  at the boundary is prescribed, the solution is determined.

The potential field is often a good approximation for the global coronal structure of the field. In active regions where high free energy is involved, however, the potential fields cannot reproduce the coronal magnetic field well.

### 1.4.2 Nonlinear force-free field

In order to reproduce the magnetic field structures in the active regions, we have to solve nonlinear equation (1.7) by numerical methods. Same as potential fields, there are several methods to solve the equation and we will use one of the methods called MHD relaxation method (section 3.2). Mikic & McClymont (1994) developed this method, which uses

zero  $\beta$  time-dependent MHD codes to achieve stationary equilibrium. Their calculation begins with the potential field calculated from the normal component of magnetic field at the photosphere, and they control the transverse electric field while keeping  $B_z$ , then finally obtain a force-free state.

In this study, we used the code developed by Inoue et al. (2014). Their code is based on the method of Mikic & McClymont (1994) and extended in two ways. First, they implemented an algorithm to remove the numerical error of  $\nabla \cdot \mathbf{B}$  proposed by Dedner et al. (2002). Second, they implemented a multigrid-type method (Brandt, 1977), which propagates the information on the boundary condition and helps achieving a force free state rapidly. We will describe the detailed numerical scheme in Chapter 3.

## 1.5 Purpose of this thesis

In this thesis, we analyze homologous flares observed by the *Hinode* spacecraft (Kosugi et al., 2007) and the *Solar Dynamics Observatory (SDO)* (Pesnell et al., 2012) in February 2014. Recently, there are a lot of studies about sheared bipole flaring active regions, while there have been little number of observational studies about other types of flares by using magnetic field data (e.g. quadrupole flares). We focus on the three-dimensional structure which caused the flares of interest. Investigating the magnetic structures responsible for the occurrence of flares is important not only in the solar physics, but also in terms of the Space Weather, which tries to predict the occurrence of flares and estimate the impact on the Earth.

The flares occurred at the quadrupole magnetic field configuration and showed homology in the EUV and UV observations. Furthermore, they showed complex post flare loops structure, which is difficult to interpret by the CSHKP model. We focus on three topics; the validity of the NLFFF modeling in this flaring region; the 3D magnetic field configuration of the flares; and the homology and the differences in three flares.

The thesis is organized as follows. In Chapter 2 we present our observations. In

Chapter 3 we show methods of our analysis and results in Chapter 4. We discuss the results in Chapter 5, and summarize our conclusions in Chapter 6.

# Chapter 2

## Observations

In this chapter, we describe the observational instruments and observational data used in this work.

We had observations of NOAA Active Region 11967 emerged on the east limb at the end of January in 2014. Figure 2.1 shows the soft X-ray fluxes on 2 February 2014 from *Geostationary Environmental Satellite (GOES)*. With the 1-8 Å flux (black in Figure 2.1), the magnitude of solar flares are classified into classes, such as C-class ( $10^{-6} \sim 10^{-5} \text{ W/m}^2$ ), M-class ( $10^{-5} \sim 10^{-4} \text{ W/m}^2$ ), and X-class ( $10^{-4} \text{ W/m}^2 \sim$ ). The Active region produced several M-class flares on 2 February. In this study we will focus on three M-class flares, which began at 08:03 (M2.2, S10E14), 09:24 (M4.4, S11E13), and 18:05UT (M3.1, S10E08). We call these flares, flare1, flare2, and flare3, respectively, in this thesis. It should be noted that the other flares, i.e., spikes in Figure 2.1, were not produced from the region of interest in the active region.

### 2.1 *Hinode* SOT Observations

On February 2, the Solar Optical Telescope (SOT; Tsuneta et al., 2008; Shimizu et al., 2008; Suematsu et al., 2008; Ichimoto et al., 2008) on board *Hinode* observed the AR 11967 in the whole day. The SOT has two focal plane instruments, i.e., the Filtergraph (FG) and the Spectropolarimeter (SP). In this thesis we use only the SP data and do not

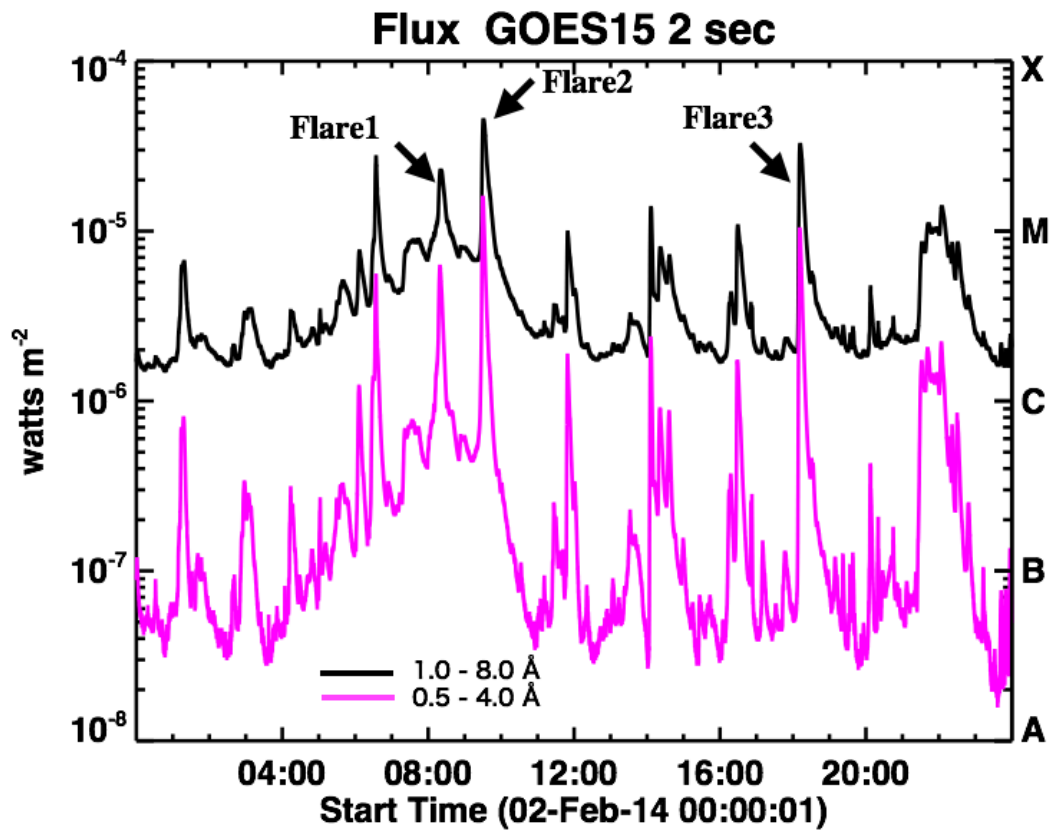


Figure 2.1: GOES X-ray fluxes showing the M-class flares on 2 February 2014. The black line shows the 1-8 Å flux and the purple line shows the 0.5-4 Å flux. Three M-class flares are focused on, which began at 07:17, 09:24, and 18:05UT.

use the FG images because of too narrow field of view.

The SP performs spectropolarimetric observations with two magnetically sensitive Fe I lines at 6301.5 Å and 6302.5 Å. The spectropolarimetric measurements produce the Stokes parameters, which are defined as follows (del Toro Iniesta, 2007),

$$\begin{aligned}
 I &= \kappa(\langle E_x^2 \rangle + \langle E_y^2 \rangle), \\
 Q &= \kappa(\langle E_x^2 \rangle - \langle E_y^2 \rangle), \\
 U &= 2\kappa\langle E_x E_y \cos \phi(t) \rangle, \\
 V &= 2\kappa\langle E_x E_y \sin \phi(t) \rangle,
 \end{aligned} \tag{2.1}$$

where  $E_x$  and  $E_y$  are the amplitude of the electric field of the electromagnetic wave in  $x$  and  $y$  direction in the Cartesian coordinates, respectively. In our analysis, the Stokes parameters are normalized by the intensity, i.e.,  $Q/I$ ,  $U/I$ , and  $V/I$ , so the value of  $\kappa$  (dimensional constant for translating  $IQUV$  into intensity units) is not so important. All the Stokes parameters have dimensions of energy. The physical meaning of the Stokes parameters is as follows. Stokes  $I$  is the total intensity of the input light; Stokes  $Q$  and  $U$  show the intensity difference of two linearly polarized components ( $0^\circ$  and  $90^\circ$  for  $Q$ ,  $45^\circ$  and  $135^\circ$  for  $U$ ); Stokes  $V$  is the intensity difference of two circularly polarized components. In practice, we measure only the intensity of the light  $I_{\text{meas}}(\theta, \delta)$  with varying observed angle  $\theta$  and phase lag  $\delta$  of the one component of  $\mathbf{E}$  with respect to the orthogonal component. The SP obtains Stokes  $IQUV$  with the polarization modulator unit (PMU) continuously rotating the waveplate in the light from the telescope. 16 images are taken in every rotation of PMU and the Stokes parameters are derived by adding and subtracting these  $I_{\text{meas}}(\theta, \delta)$  values with a modulation scheme given in Ichimoto et al. (2008). By performing the inversion of these Stokes parameters, we can estimate the magnetic field vector, the Doppler velocity, and other thermodynamic parameters (such as the Doppler width and the source function). The magnetic field data used in the thesis were obtained

with a Stokes inversion in the assumption of a *Milne-Eddington atmosphere* (section 3.1).

We use two vector magnetic field maps derived from the SP observations on 2 February 2014. The SP maps were taken with fast-mapping mode by slit scanning over almost the entire active region. Two scans were taken in two periods before flare 1 and flare 3 between 07:12 and 08:07 UT, and 16:00 and 16:52 UT. We also use the map obtained between 10:42 and 11:37UT on 1 February 2014. The maps have an effective pixel size of  $0''.3$  with a FOV of  $280'' \times 130''$ . The spectral sampling is  $21.549 \text{ m}\text{\AA} \text{ pixel}^{-1}$

## 2.2 *SDO* Observations

The Atmospheric Imaging Assembly (AIA; Lemen et al., 2012) aboard the *SDO* is used to investigate the coronal and chromospheric structures of the flaring region in the active region. The AIA has seven extreme ultraviolet (EUV) and two ultraviolet (UV) channels (Table 2.1), which observes the full disk ( $2458'' \times 2458''$ ) of the sun with a pixel size of  $0''.6$ . The temporal resolutions are 12s for EUV and 24s for UV. In this thesis, we use  $1600\text{\AA}$  for investigating the behaviors of the flare ribbons in the chromosphere and  $131\text{\AA}$  for the coronal hot plasma in the flaring region.

The Helioseismic and Magnetic Imager (HMI; Schou et al., 2012) on board *SDO* provides the full-disk photospheric magnetic field. The HMI measures polarimetric signals of magnetic sensitive Fe I  $6173 \text{ \AA}$  line at 6 narrow bands (band width  $76 \text{ m}\text{\AA} \pm 10 \text{ m}\text{\AA}$  in the line) and derive the magnetic field vectors with these polarimetric measurements.

Table 2.1: AIA Wavelength Bands

Channel Name	primary ion(s)	Char.logT (K)
white light	Continuum	3.7
1700 Å	Continuum	3.7
304 Å	He II	4.7
1600 Å	C IV + cont.	5.0
171 Å	Fe IX	5.8
193 Å	Fe XII, XXIV	6.1, 7.3
211 Å	Fe XIV	6.3
335 Å	Fe XVI	6.4
94 Å	Fe XVIII	6.8
131 Å	Fe VIII, XX, XXIII	5.6, 7.0, 7.2



# Chapter 3

## Analysis Methods

In this chapter, we describe methods of our analysis, i.e. the observational data processing, the numerical methods of NLFFF modeling developed by Inoue et al. (2014) and the squashing factor  $Q$  which is defined by Titov (1999).

### 3.1 Observational data processing

Regarding the SP data, we used the Solarsoft routine SP\_PREP (Lites & Ichimoto, 2013) for the calibration of the Stokes profiles. When we derived physical parameters from the Stokes profiles, we solved the radiative transfer equation (del Toro Iniesta, 2007),

$$\frac{d\mathbf{I}}{d\tau} = \mathbf{K}(\mathbf{I} - \mathbf{S}), \quad (3.1)$$

where  $\mathbf{I} \equiv (I, Q, U, V)$  is the Stokes vector,  $\tau$  is the optical depth,  $\mathbf{K}$  is the propagation matrix, and  $\mathbf{S}$  is the source function defined as the ratio of the emission coefficient to the absorption coefficient. As described in chapter 2, we need to assume the model atmosphere in order to derive the physical parameters (magnetic field, Doppler velocity and so on) from the Stokes profiles. In this thesis, we assumed a *Milne-Eddington atmosphere* (ME). In this atmosphere, the medium is uniform along the optical depth, and the source

function vector depends linearly on the optical depth,

$$\mathbf{S} = \mathbf{S}_0 + \mathbf{S}_1\tau, \quad (3.2)$$

There is an analytic solution of the radiative transfer equation in this atmosphere, called Unno-Rachkovsky solution (Unno, 1956; Rachkovsky, 1962). We fitted 12 free parameters (field strength, field inclination, field azimuth, doppler shift, doppler width, damping parameter, line strength, source function, source function gradient, macro turbulence, stray light fraction, and stray light shift) by a nonlinear least square fitting using the code based on MELANIE (Socas-Navarro, 2001). Although the assumption of the uniform atmosphere is not realistic, it is often a good approximation for the photosphere. In this thesis, we applied the ME model to the two lines (Fe I doublet at 6301.5Å and 6302.5 Å) and this simultaneous inversion has been shown to provide better results than using only single line (Lites et al., 1994). When deriving transverse magnetic field using Zeeman effect, there is an ambiguity called 180 degree ambiguity. In order to solve this ambiguity, we first calculated the potential field from the vertical magnetic field and selected the closer direction with the potential field. After that, we modified the transverse field using AZAM code developed by Lites et al. (1995).

The Solarsoft routine AIA\_PREP was used for AIA and HMI data calibration and alignment. We investigated coronal and chromospheric dynamics by visually checking of EUV(131Å) and UV (1600Å) data taken around the peak time of flare1 (08:00UT-09:00UT), flare2 (09:00UT-10:00UT), and flare3 (18:00UT-18:30UT).

For HMI, there is a data product, called Space-weather HMI Active Region Patches (SHARP) , which provides vector magnetic field data on a 12 minutes cadence and automatically identifies and tracks active regions (Bobra et al., 2014). We used this vector field data to increase the narrow field of view of Hinode/SP when extrapolating the coronal magnetic field by NLFFF modeling (Figure 3.1). When we make the boundary data for the modeling, we first resized HMI pixel size to the SP pixel size with a cubic poly-

mial interpolation using 16 neighboring points. The resized HMI data was co-aligned to the SP data by performing a cross-correlation technique. One of the co-aligned HMI data is shown in Figure 3.1 (a). For having a wider field of view data with higher polarimetric accuracy, the co-aligned HMI data was added to around the SP map. The  $2 \times 2$  binning data of the SP plus HMI maps, one of which is shown in Figure 3.1 (b), are used as the boundary condition for the nonlinear force-free field modeling.

## 3.2 Force-free field modeling

In order to achieve a force free state, we solved the following zero  $\beta$  MHD equations in the Cartesian coordinates (Inoue et al., 2014),

$$\frac{\partial \mathbf{v}}{\partial t} = -(\mathbf{v} \cdot \nabla) \mathbf{v} + \frac{1}{\rho} \mathbf{j} \times \mathbf{B} + \nu \nabla^2 \mathbf{v}, \quad (3.3)$$

$$\frac{\partial \mathbf{B}}{\partial t} = \nabla \times (\mathbf{v} \times \mathbf{B} - \eta \mathbf{j}) - \nabla \phi, \quad (3.4)$$

$$\mathbf{j} = \nabla \times \mathbf{B}, \quad (3.5)$$

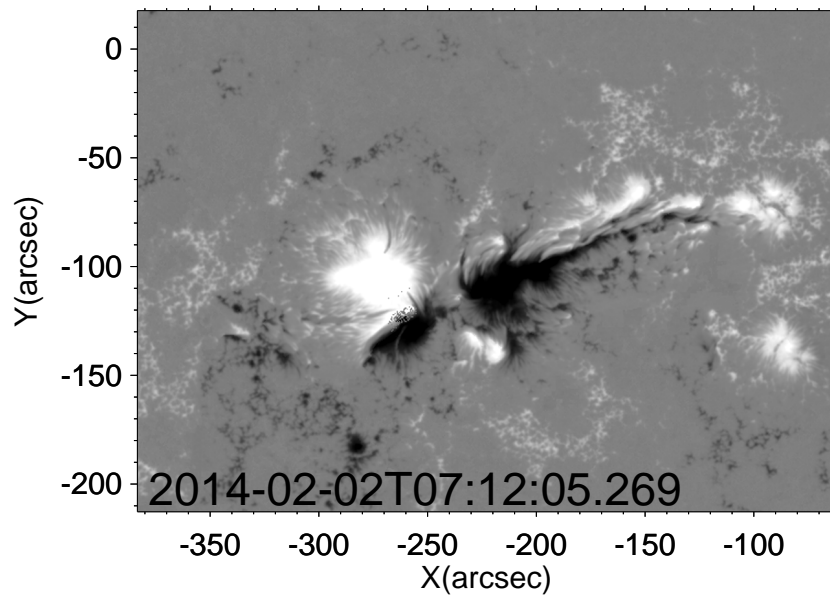
$$\frac{\partial \phi}{\partial t} + c_h^2 \nabla \cdot \mathbf{B} = -\frac{c_h^2}{c_p^2} \phi, \quad (3.6)$$

where  $\rho$  is the pseudo density, which is assumed to be proportional to  $|\mathbf{B}|$ , and  $\phi$  is the convenient potential for  $\nabla \cdot \mathbf{B}$  cleaning. Eqns. (3.3), (3.4), (3.5) and (3.6) are the equation of motion, the induction equation, the Ampère's law, and  $\nabla \cdot \mathbf{B}$  cleaning introduced by Dedner et al. (2002), respectively. The parameters  $c_p^2$  and  $c_h^2$  are the advection and diffusion coefficients, respectively and fixed at 0.1 and 0.04. The non-dimensional resistivity  $\eta$  is given by

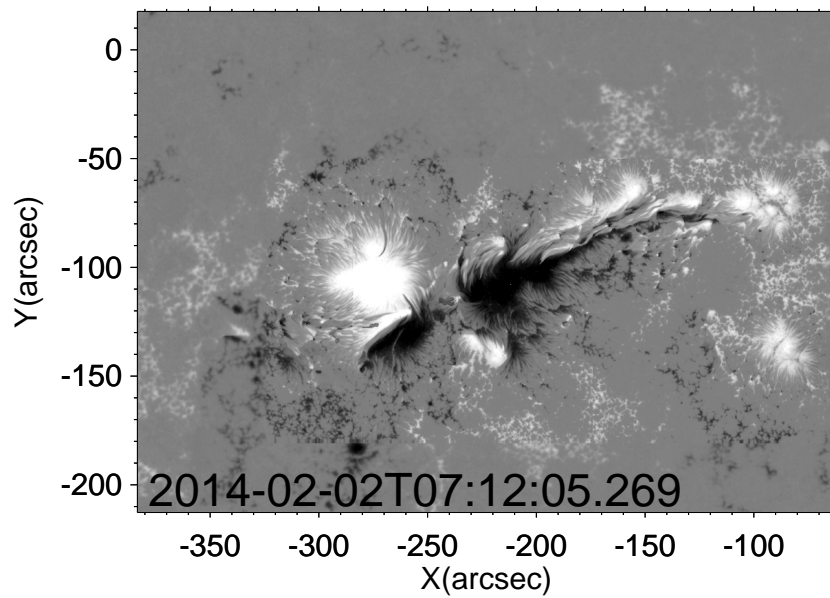
$$\eta = \eta_0 + \eta_1 \frac{|\mathbf{j} \times \mathbf{B}| |\mathbf{v}|^2}{|\mathbf{B}|^2}, \quad (3.7)$$

where  $\eta_0$  and  $\eta_1$  are fixed at  $5.0 \times 10^{-5}$  and  $1.0 \times 10^{-3}$  in non-dimensional units.

The initial condition was the potential field calculated from the normal component of the observed magnetic field and the calculation used Green's function method (Schmidt,



(a)



(b)

Figure 3.1: (a) The vertical magnetic field by *SDO/HMI*, (b) The vertical magnetic field by *Hinode/SOT* with increasing the field of view with *SDO/HMI*. The map in (b) was used in the nonlinear force-free field modeling.

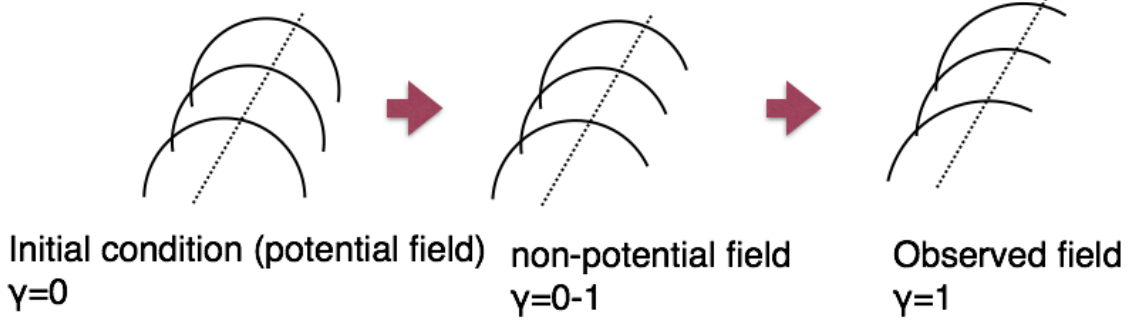


Figure 3.2: The concept of the method of Inoue et al. (2014). We set the potential field as an initial condition and solved zero- $\beta$  MHD equations with varying the bottom boundary condition according to eqn. (3.8).

1964) . The magnetic field at the top and side boundaries was fixed and the normal component of the magnetic field on the bottom boundary was also fixed. We varied the transverse component on the bottom boundary  $B_{BC}$  as follows,

$$B_{BC} = \gamma B_{obs} + (1 - \gamma) B_{pot} \quad (3.8)$$

where  $B_{obs}$  and  $B_{pot}$  are the transverse component of the observational and potential fields, respectively. We increase  $\gamma = \gamma + d\gamma$  when  $\int |\mathbf{j} \times \mathbf{B}|^2 dV$  drops below a critical value. In this study we set  $d\gamma = 0.1$  and when  $\gamma$  becomes equal to 1,  $B_{BC}$  is consistent with the observed field (Figure 3.2).

Spatial derivatives are calculated by the second-order central differences and temporal derivatives are integrated by the Runge-Kutta-Gill method to fourth order accuracy. We used the combined SP and HMI data as the boundary condition on the bottom, which is shown in Figure 3.1 (b). The numerical domain is set to  $(0, 0, 0) < (x, y, z) < (1.5, 1.0, 0.5)$  resolved by  $540 \times 360 \times 180$  nodes.

We used UCAR's Vapor three-dimensional visualization package ([www.vapor.ucar.edu](http://www.vapor.ucar.edu)) in order to visualize the field lines.

### 3.3 Squashing factor

In order to define QSLs, the norm  $N$  has been proposed (Priest & Démoulin, 1995; Démoulin et al., 1996), which is,

$$N = \sqrt{\left[ \left( \frac{\partial X}{\partial x} \right)^2 + \left( \frac{\partial X}{\partial y} \right)^2 + \left( \frac{\partial Y}{\partial x} \right)^2 + \left( \frac{\partial Y}{\partial y} \right)^2 \right]}, \quad (3.9)$$

where  $(X, Y)$  is another footpoint of the field line connecting from a selected footpoint at  $(x, y)$ .  $N$  is the norm of the displacement gradient tensor and evaluated only on the boundary. They claimed that QSLs exist at the locations of high  $N$  shown in Figure 3.3.  $N$  is non-dimensional and independent of the coordinate system. There is, however, a problem in the norm to define QSLs. If we calculate the norm at different footpoints of the same field line, the values are generally different, making it ambiguous to determine the QSLs. To solve this problem, the new definition of QSLs called squashing factor  $Q$  is proposed by Titov (1999) and improved in later studies (Titov et al., 2002; Titov, 2007; Pariat & Démoulin, 2012). The squashing factor  $Q$  is defined as

$$Q = \frac{N^2}{\Delta}, \quad (3.10)$$

where Jacobian matrix  $D$  of the field-line mapping and its determinant  $\Delta$  is

$$D = \begin{pmatrix} \partial X/\partial x & \partial X/\partial y \\ \partial Y/\partial x & \partial Y/\partial y \end{pmatrix} = \begin{pmatrix} a & b \\ c & d \end{pmatrix}, \quad (3.11)$$

$$\Delta = ad - bc. \quad (3.12)$$

The meaning of the squashing factor  $Q$  is a product of the norms  $N_+$  and  $N_-$ , which is calculated from each footpoint of the same field line,

$$N_+ = N, \quad N_- = \frac{N}{\Delta}. \quad (3.13)$$

Therefore,  $Q$  calculated from the footpoints of the same field line has a same value. Titov et al. (2002) showed that the determinant of Jacobian matrix ( $\Delta$ ) is related to the ratio of the normal component of magnetic field on the boundary,

$$|\nabla| = \frac{|B_{z,+}|}{|B_{z,-}|}. \quad (3.14)$$

Although the squashing factor  $Q$  is originally defined only on the boundary, Pariat & Démoulin (2012) extended it in a 3D domain assuming the squashing factor is invariant along a field line.

By using eqns. (3.10) and (3.14), we calculated the squashing factor in a 3D domain using the results of the force-free modeling. We integrated the field lines with fourth-order Runge-Kutta method and chose the step size by adaptive step size control.

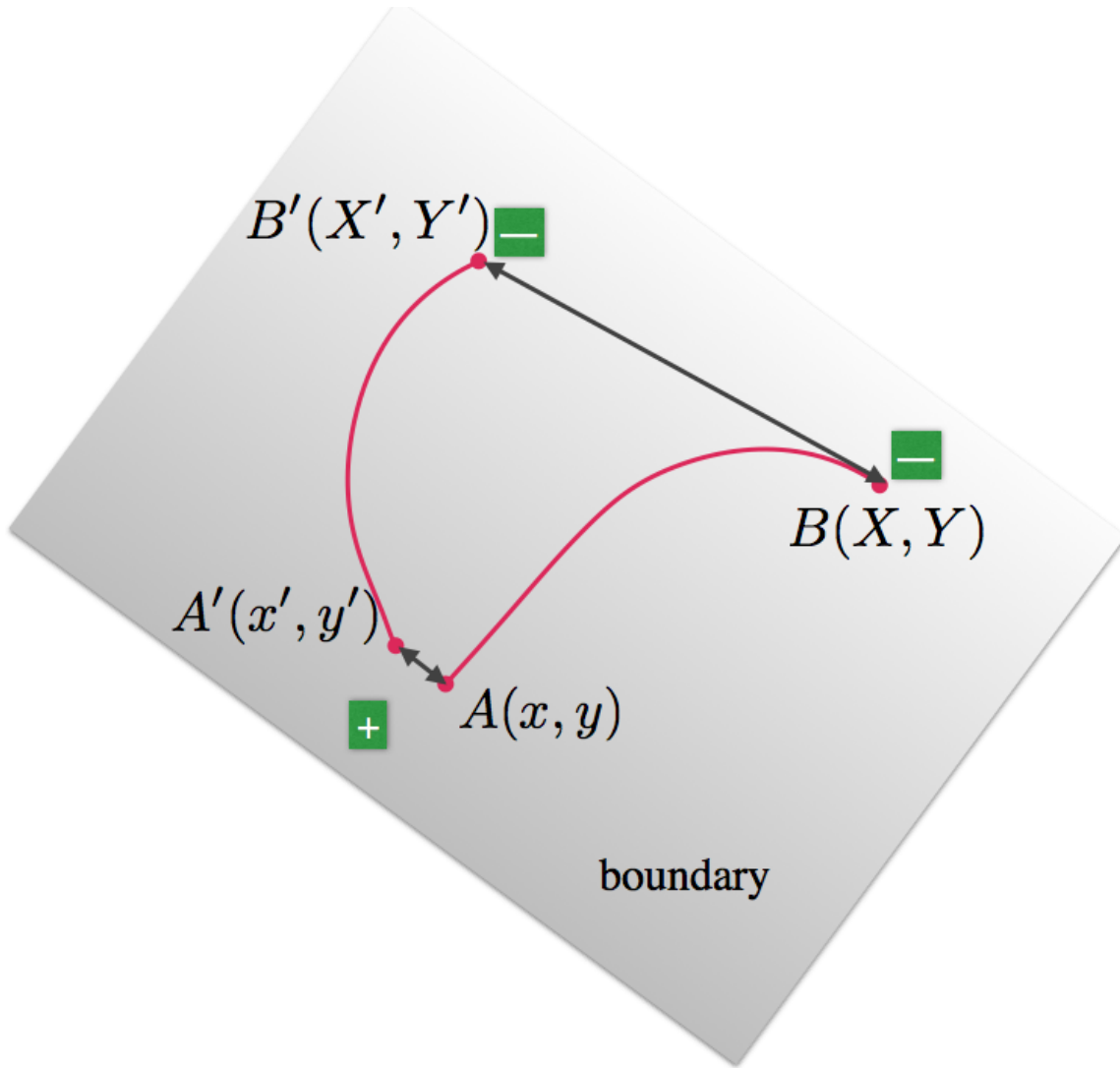


Figure 3.3: The sketch of the norm  $N$ . The norm expresses the ratio of footpoint distance, i.e., the ratio of the distance  $AA'$  to  $BB'$ .



# Chapter 4

## Results

In this chapter, we provide the results from the data analysis with the nonlinear force-free modeling and squashing factor described in chapter 3.

### 4.1 Properties of the flares from observations

#### 4.1.1 Flare ribbons, post flare loops, and photospheric magnetic fields

AIA 1600 Å images provide where heating events take place in the chromosphere. When flares occur, flare ribbons appear in the chromosphere and they correspond to the foot-points of flare loops. Figure 4.1, 4.2, and 4.3 show the AIA 1600Å images observed during flare1, flare2, and flare3, respectively, with the time plot of the *GOES* X-ray flux. Red circles in the time plots give the observed timing of each UV image.

Flare 1 began at 08:03UT (Figure 4.1 (a)), and four flare ribbons appeared in the north part of the active region in the main phase (Figure 4.1 (c)). The X-ray flux gradually increased in the period from (a) to (b) and then increased in a short time toward (c). We can see a loop-like structure in Figure 4.1 (a), which is clearly seen in EUV shown later. In Figure 4.1 (b), we can identify the initial localized kernels of the flare ribbons located at two sunspots, while at the main phase of the flare in Figure 4.1 (c), bright points were located in the plage region.

Flare 2 and 3 show flare ribbons similar to flare 1 in 1600 Å and thus they are recognized as homologous flares. It is noted that the temporal evolution of the X-ray flux in flare 2 and flare 3 shows different behavior from that of flare 1, that is, there is only one impulsive increase in the X-ray flux without a gradual increase as shown in the bottom panel of Figure 4.2 and 4.3. Both flare 2 and flare 3 show four flare ribbons identified in the main phase. However their flare kernels in the initial phase show different behavior. In the case of flare 1, the bright points are recognized at the two sunspot, but in flare 2, we can see four kernels in total, two of which are located at two sunspots and the other two at plage in Figure 4.2 (a). Flare 3 shows more than four bright kernels in the initial phase and also show a loop-like structure. Differences in the number and the location of bright kernels among these flares will be discussed in chapter 5.

Figure 4.4 shows the line-of-sight magnetograms from *SDO/HMI* at the time of each flare. The color contours show the bright regions in the flare ribbons at the start of impulsive increase in X-ray flux, which correspond to the intensity level higher than 5000 DN in AIA 1600 Å in Figure 4.1 (b), 4.2 (a) and 4.3 (a), respectively. The bright regions are distributed in four magnetic polarities, meaning that magnetic field lines from these bright regions reconnect and release energy. The four magnetic polarities are labeled as P1, N1, P2, and N2 (as shown in the cartoon in the right bottom panel of Figure 4.4 ). P1 and N1 correspond to positive and negative sunspot regions (3000~4000 G), respectively, while P2 and N2 are in plage regions (~1500G). We will show three dimensional coronal magnetic structure formed above the photospheric distribution of these magnetic polarities later in this chapter.

Figure 4.5 shows the temporal evolution of vertical magnetic flux observed with HMI from 1 February to 3 February 2014. There can be clearly seen flux emergences in the regions of the red box and the yellow box. The two sunspots P1 and N1 show the converging motion during two days as shown by the light blue arrow (around 7000 km in two days).

We measured the temporal evolution of vertical magnetic flux of the four region using

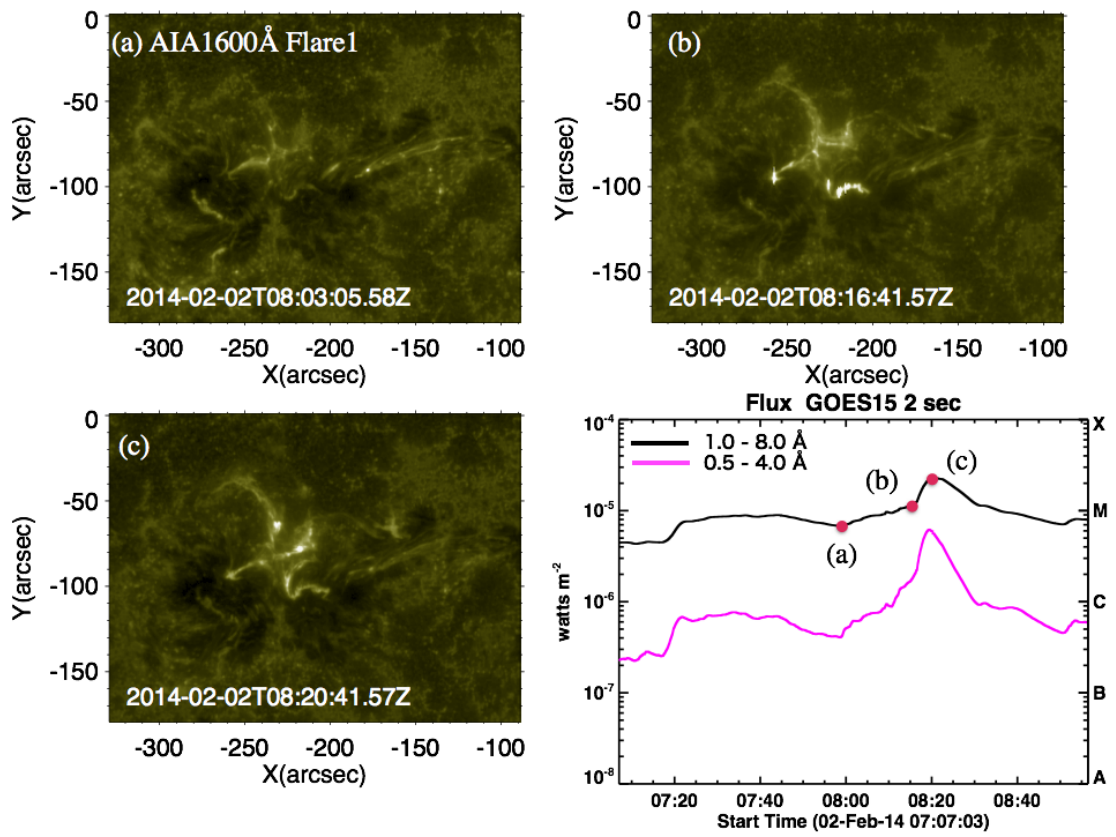


Figure 4.1: Images of AIA 1600 Å for flare 1. The right bottom panel shows *GOES* X-ray flux. The observed time in (a), (b), and (c) images corresponds to the time of each red circle in the right bottom panel.

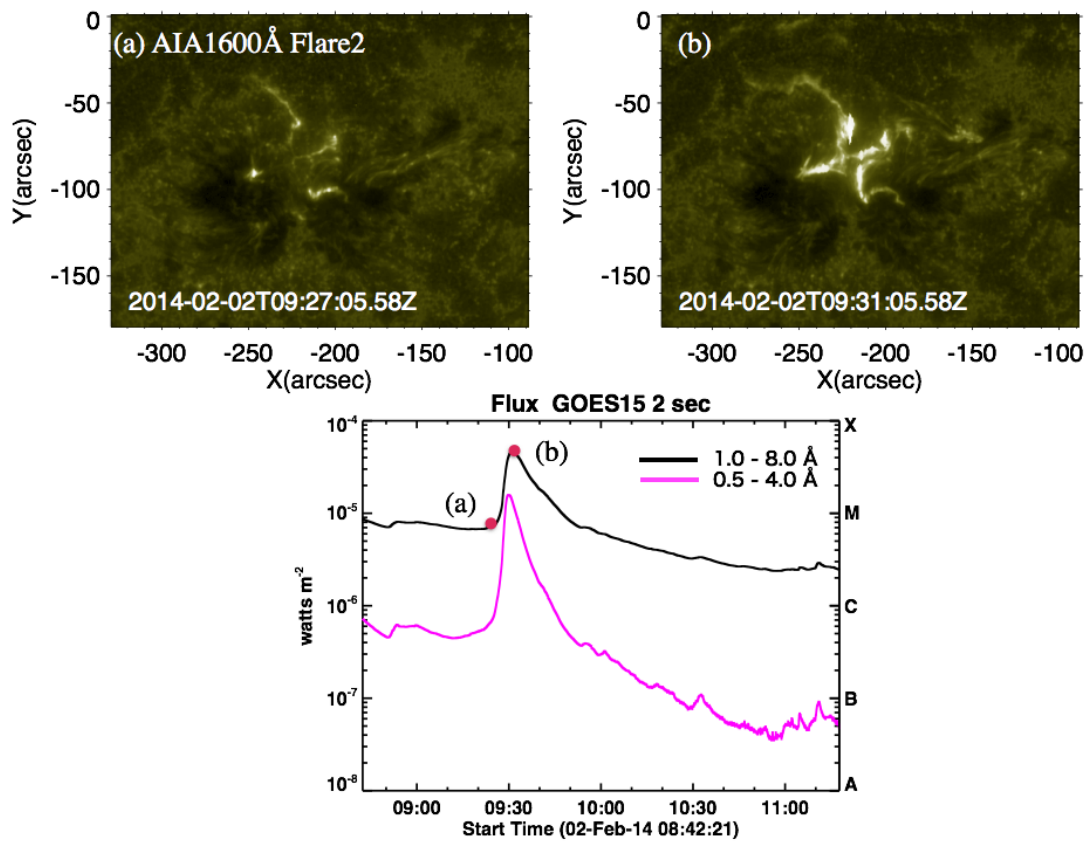


Figure 4.2: Images of AIA 1600 Å for flare 2. The bottom panel shows *GOES* X-ray flux. The observed time in (a) and (b) images corresponds to the time of each red circle in the bottom panel.

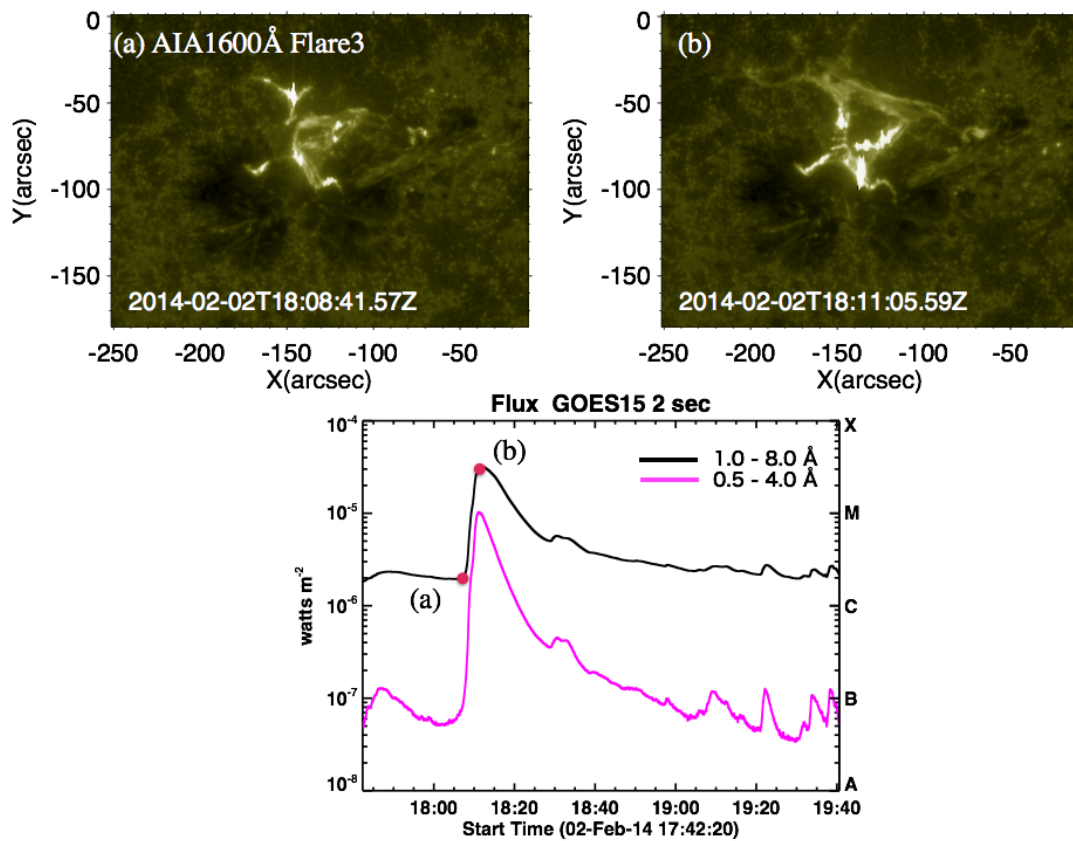


Figure 4.3: Images of AIA 1600 Å for flare 3. The bottom panel shows *GOES* X-ray flux. The observed time in (a) and (b) images corresponds to the time of each red circle in the bottom panel.

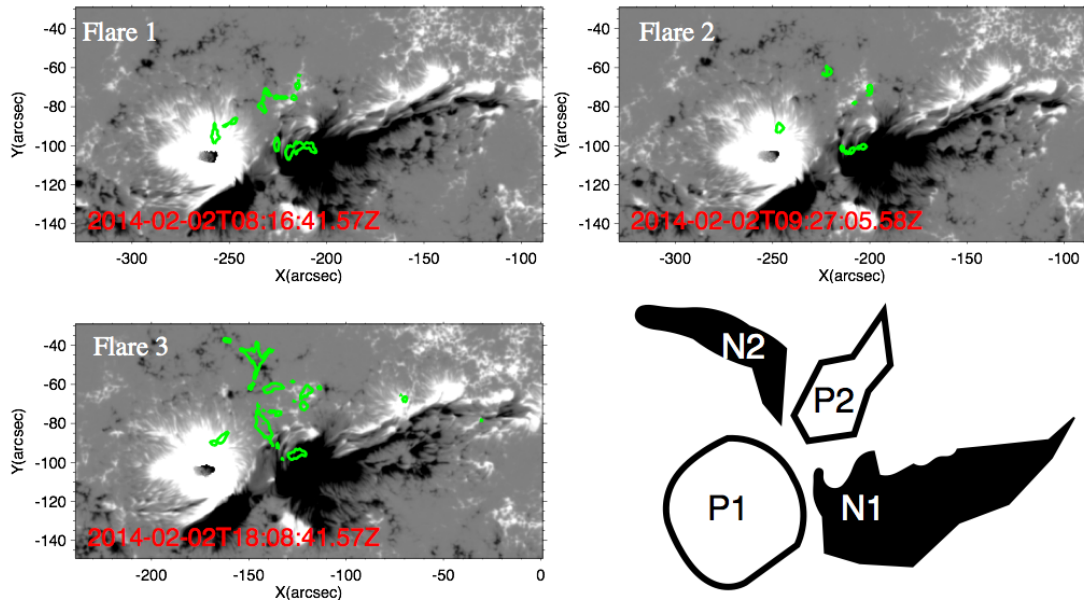


Figure 4.4: Line of sight component of magnetic field strength observed by HMI around flare 1, flare 2, and flare 3. Green contours show flare ribbons in AIA 1600 Å. The right bottom sketch describe the magnetic field polarity where the flare ribbons were observed.

HMI 12 minutes cadence data as shown in Figure 4.6. Colored box in the upper panel show the measured regions. Red, blue, green, and orange boxes are correspond to P1, N1, N2, and P2, respectively. The colored lines in the bottom panel correspond to each of the region. While the magnetic fluxes of P1, P2, and N2 do not change drastically, that of N2 increases more than  $5.0 \times 10^{21}$ Mx during the day.

The EUV 131 Å images observed by *SDO/AIA* for the three flares are shown in Figure 4.7, 4.8, and 4.9, which provide the information of coronal plasmas in high temperature (Table 2.1) during the flares. The footpoints of the flare loops are located at the photospheric magnetic field regions labeled P1, P2, N1, and N2.

In flare 1, the P1-N1 loop can be seen dominantly before the time of the main energy release (Figure 4.7 (a)). The P1-N1 and P2-N2 loops, drawn by dotted lines in Figure 4.7 (b) were observed in the main phase. After the main phase, instead of the P2-N2 structure, the P1-N2 and P2-N1 structures appeared with the pre-existing P1-N1 structure as seen in Figure 4.7 (c).

In flare 2 and flare 3, the P1-N1, P1-N2, and P2-N1 structures are visible after the

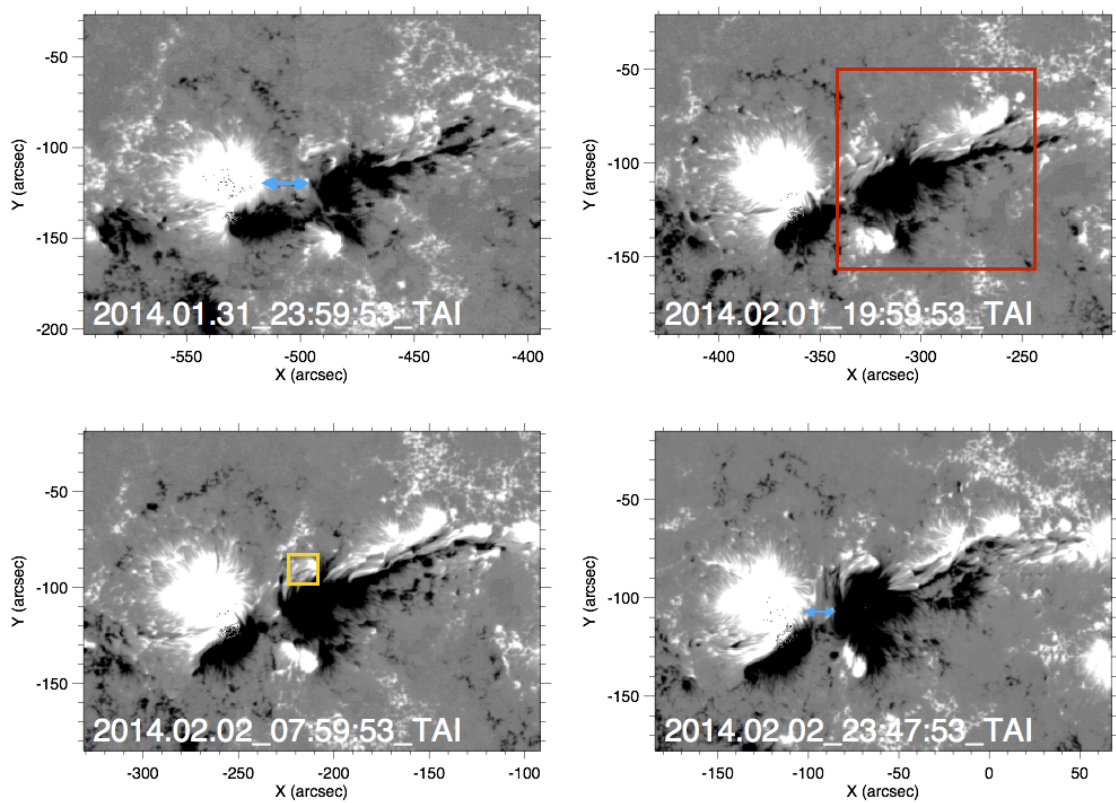


Figure 4.5: Images of the temporal evolution of the vertical magnetic flux observed with HMI. The red and yellow boxes show the region of the flux emergence and the light blue arrows show the converging motion of the sunspots.

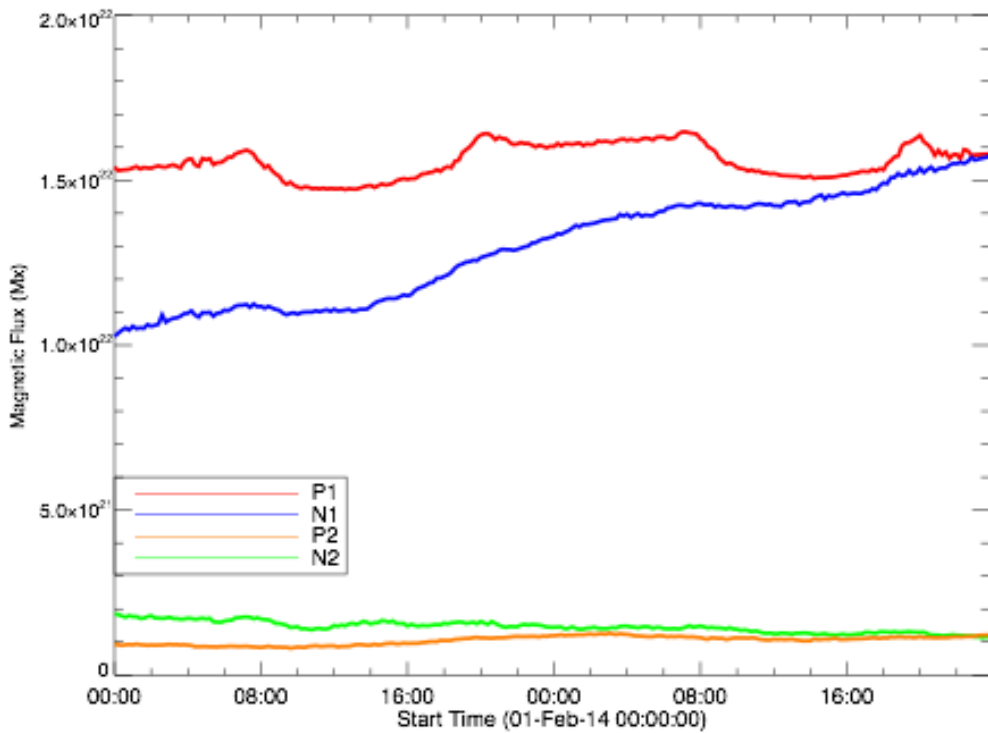
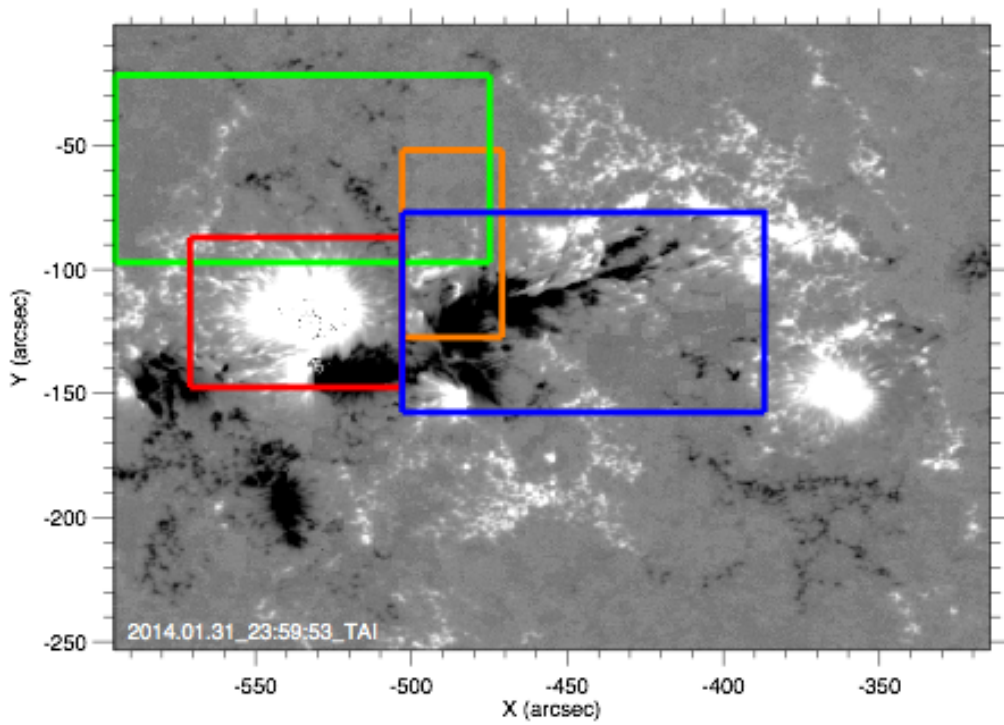


Figure 4.6: Temporal evolution of vertical component of magnetic flux in the period of 1 to 2 February 2014 is shown in the bottom panel. The regions around P1, P2, N1, and N2 were measured, which correspond to the red, orange, blue, and green box of the upper panel, respectively.

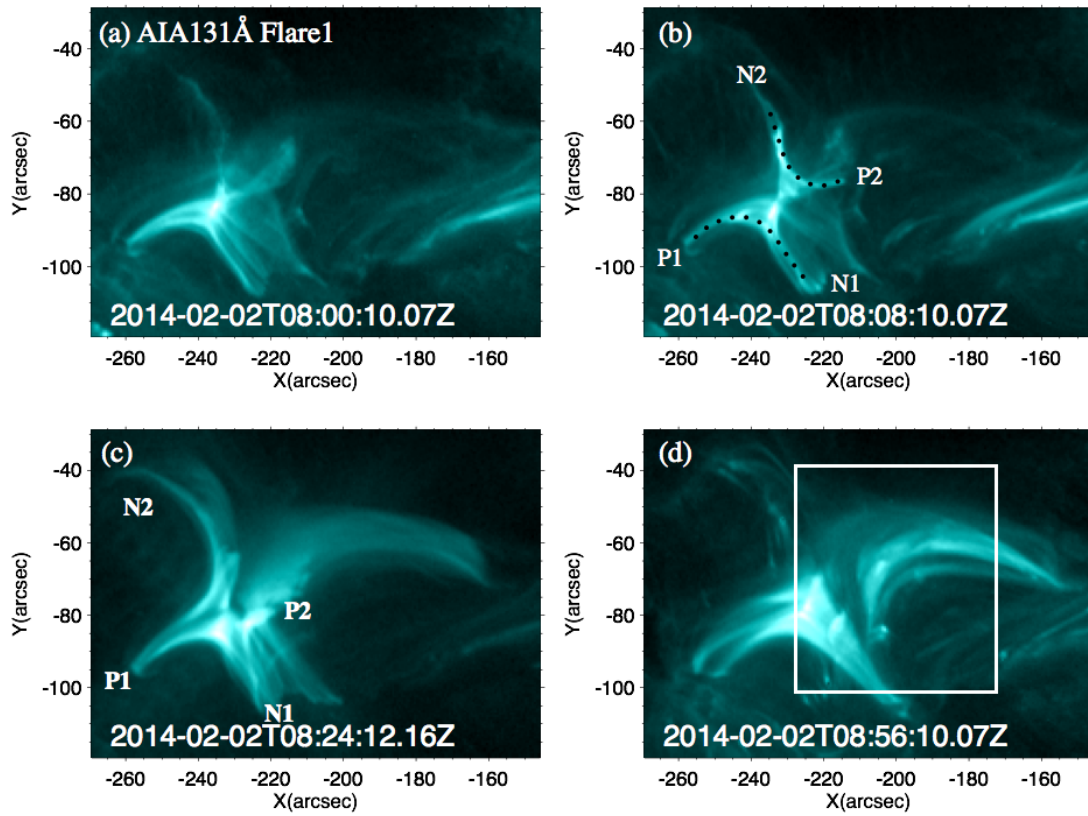


Figure 4.7: Images of AIA 131Å for flare 1. Black dotted line in panel (b) shows the bright structure in the image and polarities of each footpoint are shown in (b) and (c). A white box shows the location of a dark ejecting material.

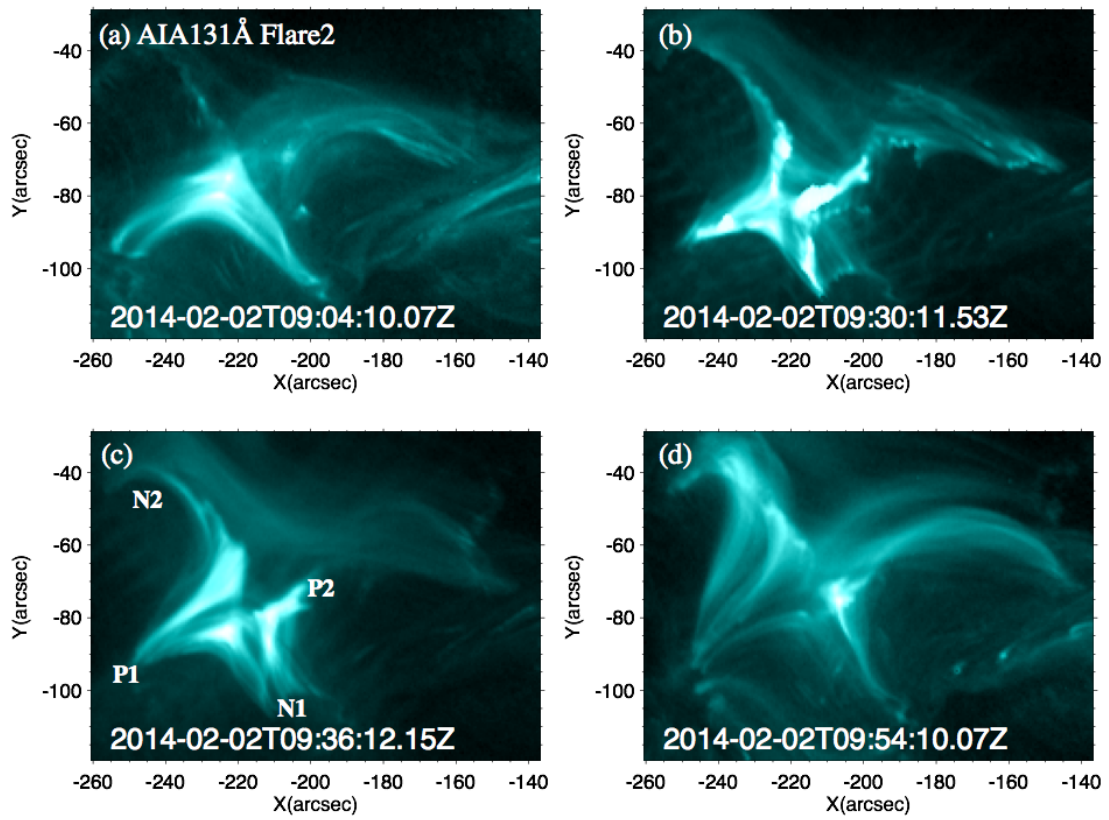


Figure 4.8: Images of AIA 131Å for flare 2. Polarities of each footpoint are shown in (c).

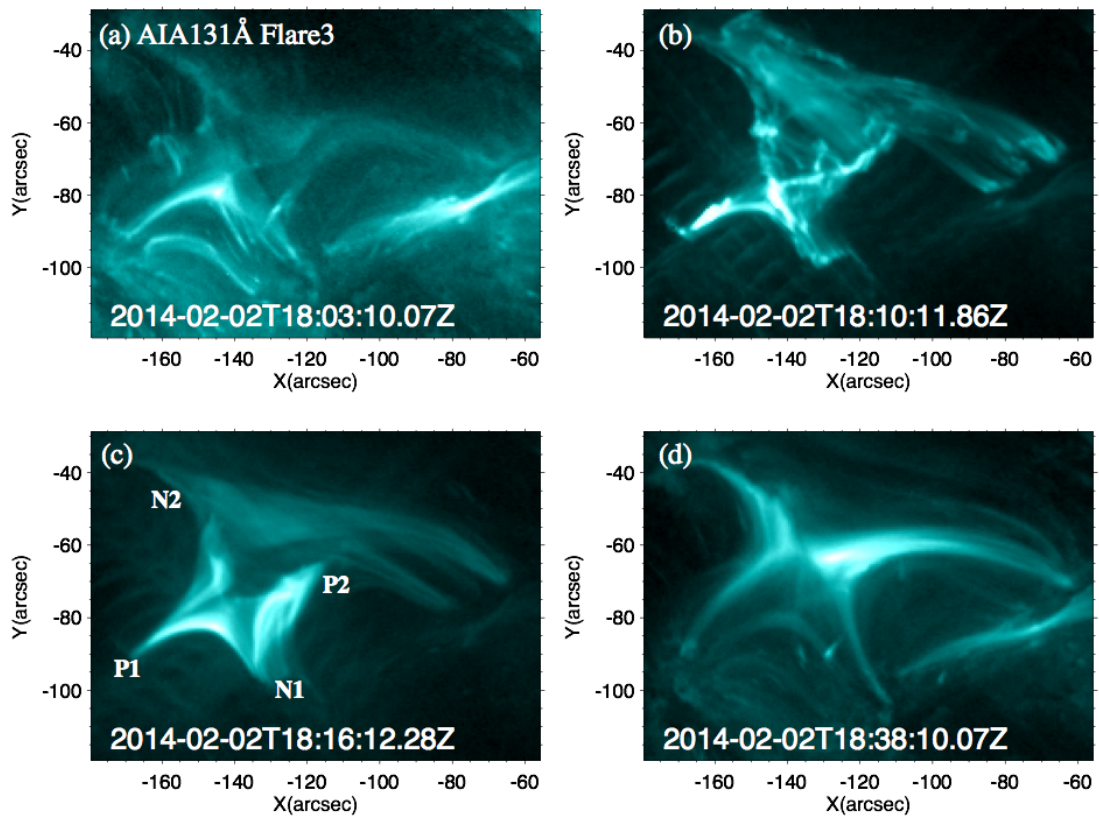


Figure 4.9: Images of AIA 131Å for flare 3. Polarities of each footpoint are shown in (c).

main phase (Figure 4.8 (c) and 4.9 (c)). We cannot recognize the structure connecting P2 to N2 before the main phase, which is different from flare 1 (Figure 4.7 (b)).

The significant changes in the connectivity of X-ray bright structures around the time of the main energy release suggest the magnetic reconnection in the coronal magnetic structures formed above the quadrupole magnetic polarity distribution. The common observed features in the three flares are the appearance of three post-flare bright structures in 131 Å images: P1-N1, P1-N2 and P2-N1. However, it is difficult to imagine how the three bright structures are formed with magnetic reconnection. A cusp-shaped structure was clearly observed in Fig. 4.8 (c) (P1-N1) and in Fig. 4.9 (d) (P2-N1 and P1-N2). In terms of the CSHKP model in 2D, we cannot predict such complex post flare loops structure. These complex structures may attribute to the reconnection in three dimensional structure of the magnetic field. We will show reconnection region using force-free field modeling later in this chapter.

### 4.1.2 Preflare activities

Triggering the flares is not clearly identified with the data, but there are some candidates for triggering. There are some noticeable events observed before flare 1 and flare 2. In flare 1, there was another event starting from around 07:17UT at the east of the flare 1 location as shown in Figure 4.10.

The end of the flare 1 (square in the fourth column of Fig. 4.7), an ejecting dark material was observed, which may trigger the following flare 2. We can see the dark material 30 minutes before flare 2 as shown in Figure 4.11. The material was not ejected to the space and returned to the surface of the sun. The upward motion of the material contributed to lifting up the overlying loop. This ejection might help reducing the magnetic tension from the overlying loop.

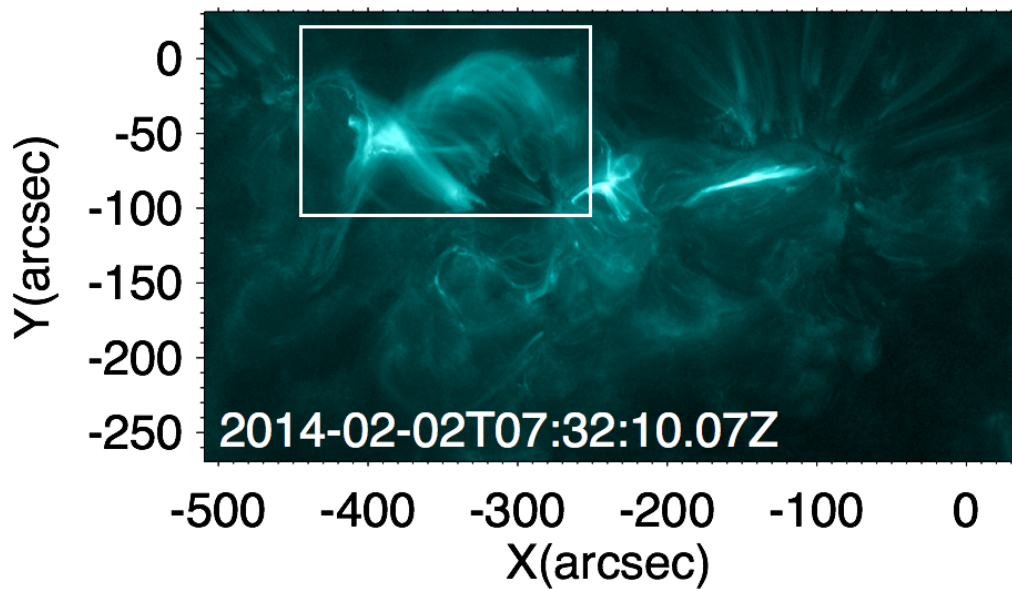


Figure 4.10: AIA 131 Å image observed 30 minutes before flare 1 started. A White box shows the region of another event which occurred before flare 1

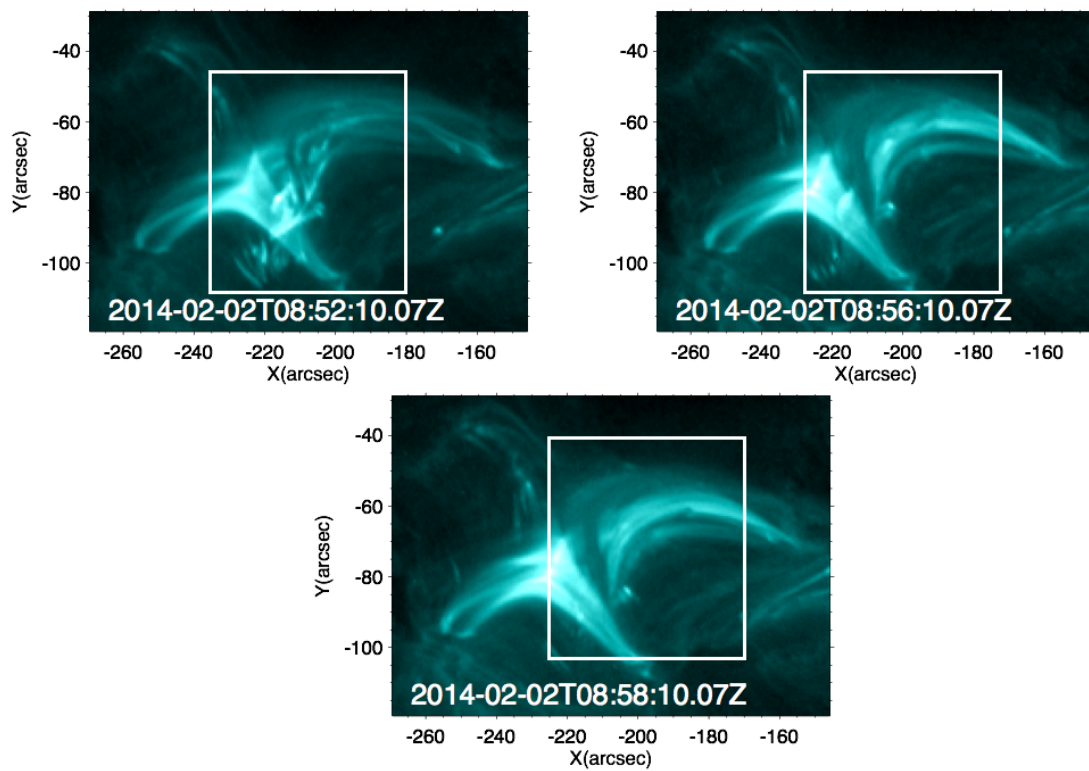


Figure 4.11: Images of AIA 131 Å after flare 1. The ejecting material surrounded by the white box was observed. This material could not eject to the space and return to the solar surface. About 30 minutes after this ejection, flare 2 occurred.

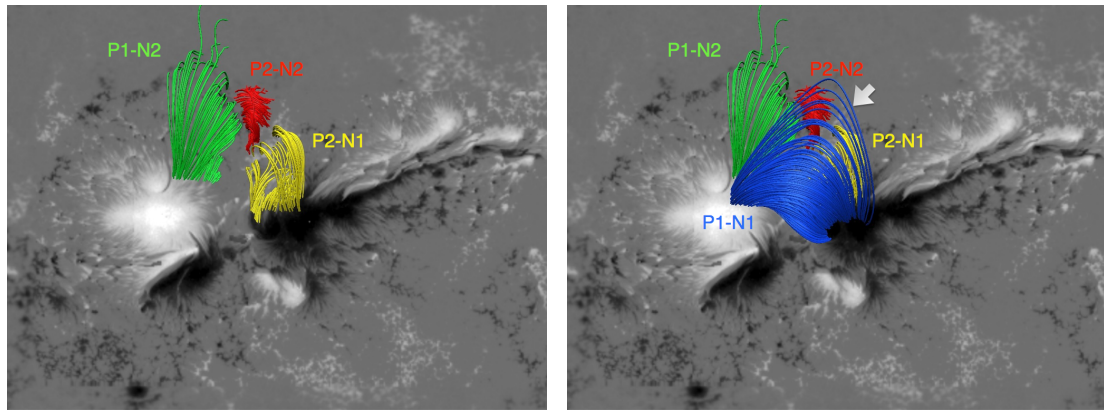
## 4.2 3D magnetic field structure in the corona

### 4.2.1 Distribution of magnetic field lines in the flaring region

Figure 4.12 shows the results from the force-free field modeling based on the SP data obtained between 07:12 and 08:07UT on 2 February 2014, which is about one hour before the occurrence of flare 1. Color lines give magnetic field lines. The background map shows the vertical component of the magnetic field. The field lines are drawn from randomly selected points in each region. Each color of field line expresses each connectivity of the field. The P1-N1, P1-N2, P2-N2, and P2-N1 connectivity correspond to blue, green, red, and yellow lines, respectively. Figure 4.12 (a) and (b) are a bird's view from the same direction. In Figure 4.12 (a), the field lines of the P1-N2, P2-N1, and P2-N2 are drawn and P1-N2 is added in Figure 4.12 (b). Figure 4.12 (c) shows the three dimensional field configuration by showing another bird's view from a different direction, which is given by the white arrow in Figure 4.12 (b).

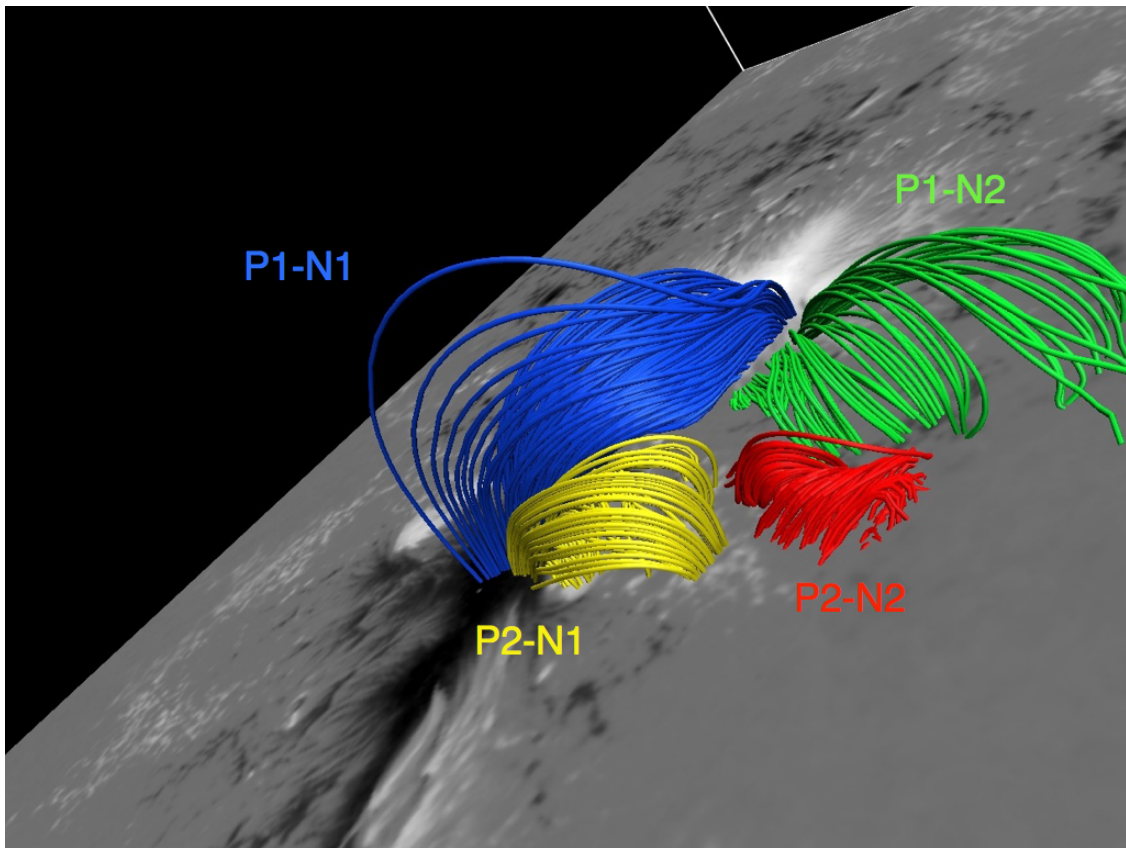
The force-free field modeling reveals four sets of connectivities in the magnetic field lines originated in the four flare ribbons. The P1-N1 field lines are rather tall and located above the other field lines (P1-N2, P2-N1, and P2-N2). There is a null point like structure in the center of the four field connections, whose height is around 2000 km. This height is located in the chromosphere and the transition region.

Figure 4.13 shows the magnetic field structure above the regions of our interest. The background grayscale shows the vertical magnetic field obtained by the SP between 07:12 and 08:07UT with increasing the field of view with *SDO/HMI*. Red lines show field lines around the flares, which we focus on. Blue lines show the field lines above the red field lines and the region pointed by the white arrows corresponds to another event occurring 30 minutes before flare 1 shown in Figure 4.10. As shown in the next section, the field connectivity derived from the NLFFF modeling is well matched to observations for low-lying structures. On the other hand, the larger scale structure of overlying magnetic field



(a)

(b)



(c)

Figure 4.12: The results of the force-free field modeling. Magnetic field lines are drawn by colored lines. In the panels (a) and (b), top is north and right is west. The panel (a) shows the magnetic field lines of P1-N2, P2-N2, and P2-N1. The panel (b) adds the field lines of P1-N1 to the panel (a). The panel (c) shows the same field lines with (b) but it is viewed from the direction given by the white arrow in (b).

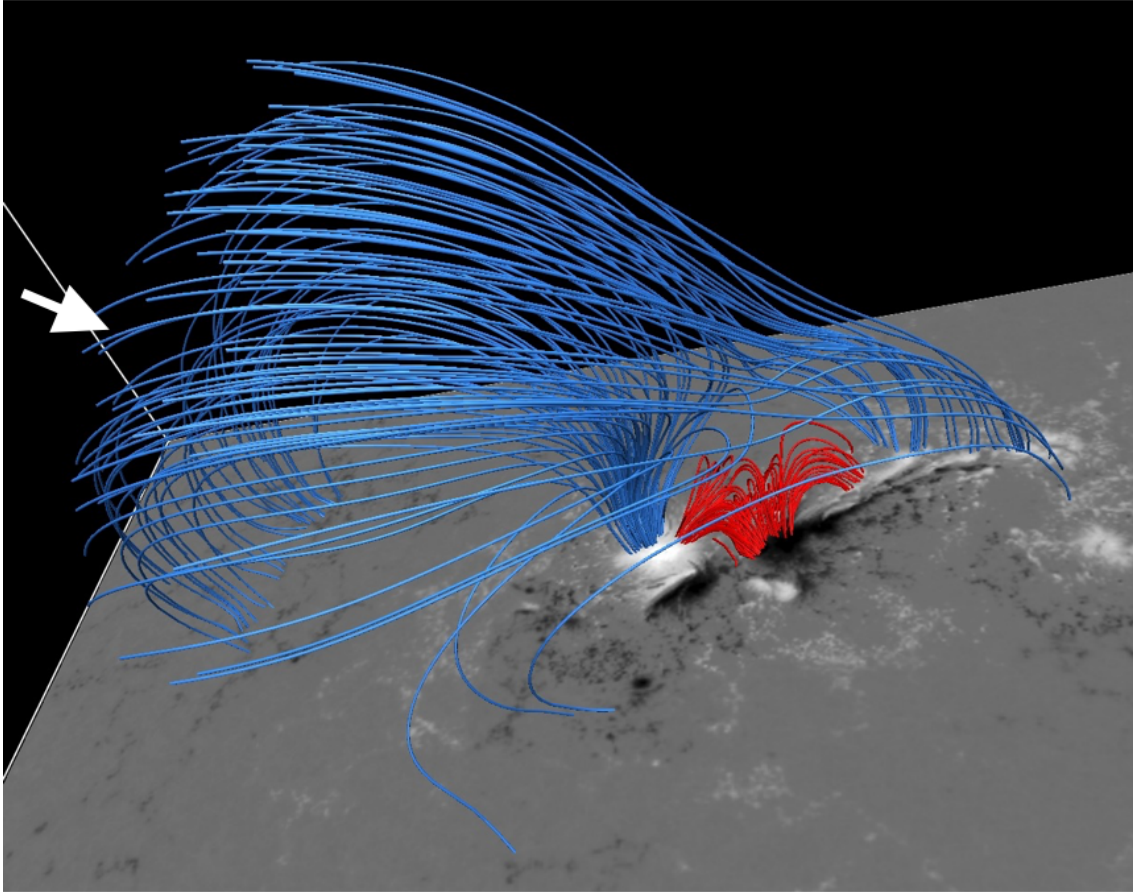


Figure 4.13: The results of force-free field using magnetic field obtained by the SP between 07:12 and 08:07UT with increasing the field of view with HMI observed at 07:12UT on 2 February 2014. Red lines show field lines around the flares, which we focus on. Blue lines show the field lines above the red field lines and the region pointed by the white arrows corresponds to another event occurring 30 minutes before flare 1 shown in Figure 4.10.

(blue lines in Figure 4.13) may not be reproduced well. This is because the blue fields are rooted into the box boundary. Thus the magnetic field lines given in Figure 4.13 should be considered just for roughly understanding the overall magnetic field configuration.

## 4.2.2 Comparisons with observations

Figure 4.14 shows an AIA 131 Å image (lower panel) taken during flare 1 and the coronal magnetic field lines from the NLFFF modeling with the vertical component of the magnetic field ( $B_z$ , upper panel). Both figures are co-aligned each other and magnetic

field lines from the region of interest at the photosphere are shown by light blue lines. Apparently, the P1-N1 field lines (white dotted line in the upper panel) are similar to the observed bright flare structure and the field line from the west side of the N1 sunspot (yellow dotted line) shows also similar shape in the coronal 131 Å image. Note that the brightening loops seen in the AIA image appeared as a result of magnetic reconnection, so the shape of the brightening structures is not necessarily same with the shape of coronal magnetic fields from the NLFFF modeling.

The connectivity of magnetic field lines from the location of kernels in the flare ribbons was also examined (Figure 4.15 and 4.16). We present only the cases of flare 1 (Figure 4.15) and flare 3 (Figure 4.16) because the SP data does not exist in the period of between flare 1 and flare 2. The grayscale background images show the vertical magnetic field, which are obtained between 07:12 and 08:07UT (Figure 4.15; one hour before flare 1) and between 16:00 and 16:52UT (Figure 4.16; 2 hours before flare 3). The overlaid color images show the bright footpoints (in red) in the AIA 1600 Å at the initial phase of each flare (corresponding to the time of Figure 4.1 (b) and Figure 4.3 (c), respectively). The upper panel shows the AIA 1600 Å bright footpoints overlaid on the vertical magnetic flux distribution, while the middle and bottom panels show the magnetic field lines from bright kernels (yellow, green and blue lines, corresponding to P2-N1, P1-N2 and P1-N1, respectively).

In flare 1 (Figure 4.15), the magnetic field lines with green are from a tiny kernel in the positive polarity sunspot and they are connected to the flare ribbon in the plage region (N2). The magnetic field lines with blue are from a bright kernel in the same positive polarity sunspot and they are connected to the negative polarity sunspot (N1). In flare 3 (Figure 4.16), the bright kernel was observed in sunspot P1 and the magnetic field lines from the kernel are connected not only to N2 in the place but also N1 in the negative spot. The data show that bright kernels existed at the other ends of the magnetic field lines from the kernels in sunspot N1, indicating that the NLFFF modeling reproduces the coronal magnetic fields well matched to the coronal morphology. The counterpart of the

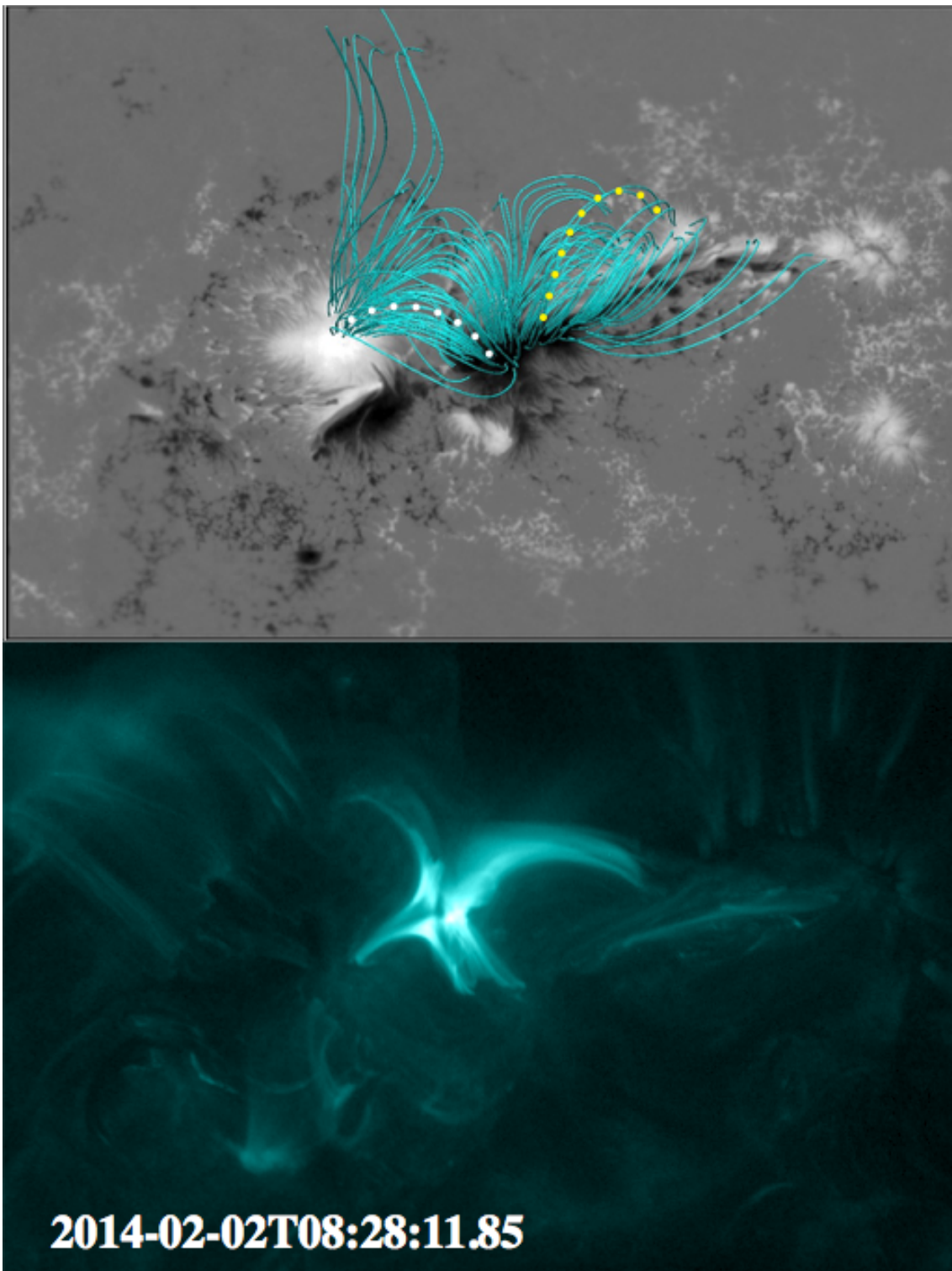


Figure 4.14: The comparison of the NLFFF modeling and an image of AIA 131 Å. Both images are co-aligned each other. The upper panel shows the vertical magnetic field by gray scale and the magnetic field lines by light blue lines. The bottom panel shows the AIA 131Å image. White and yellow dotted lines show the similar structure with the observation.

yellow field lines from the yellow box in Figure 4.15 are also rooted in the kernel region (N1). Note that the yellow box is a positive polarity magnetic island without showing any bright points. The similar connectivity was observed in Figure 4.16 for the magnetic field lines from the yellow box. Nearby magnetic flux next to the bright kernel in N1 has the connection to kernels in the P1 plage. This connectivity is more evident in Figure 4.16. In Figure 4.16, another bright flare footpoint was observed apart from the flaring region discussed so far at the west edge of the frames. The magnetic field lines from this region (another yellow field lines from the red box) are rooted in a non-flaring region in the N1 region. This loops may correspond to a bright coronal structure at the west side of the flaring region as seen in Figure 4.9. We will discuss the validity of the NLFFF modeling in chapter 5.

## 4.3 Quasi-Separatrix Layers

### 4.3.1 Spatial distribution of the QSLs

Using the 3D magnetic field data from the nonlinear force-free field modeling, the squashing factor  $Q$  defined in section 3.3 was derived. Figure 4.17 shows the spatial distribution of  $Q$  in logarithmic scale calculated from the result shown in Figure 4.12. The upper panel shows the  $\log Q$  map at  $\sim 800$  km above the photosphere (the formation layer of Fe I lines). This height is in the chromosphere where the flare ribbons are observed, allowing us to compare the chromospheric location of QSLs with the location of the flare ribbons. The lower panel in Figure 4.17 shows the chromospheric location of high  $Q$ , exactly  $\log Q > 1$ , which is given by purple. Green contours give the bright footpoint in AIA 1600 Å, same as the upper left panel in Figure 4.4. An X like shape is visible around the center of the quadrupole structure ( $X \sim -245$  arcsec,  $Y \sim -85$  arcsec).

The location of the highest squashing factor around the flaring region is important in discussing the reconnection site. Figure 4.18 shows the vertical distribution of  $\log Q$  in

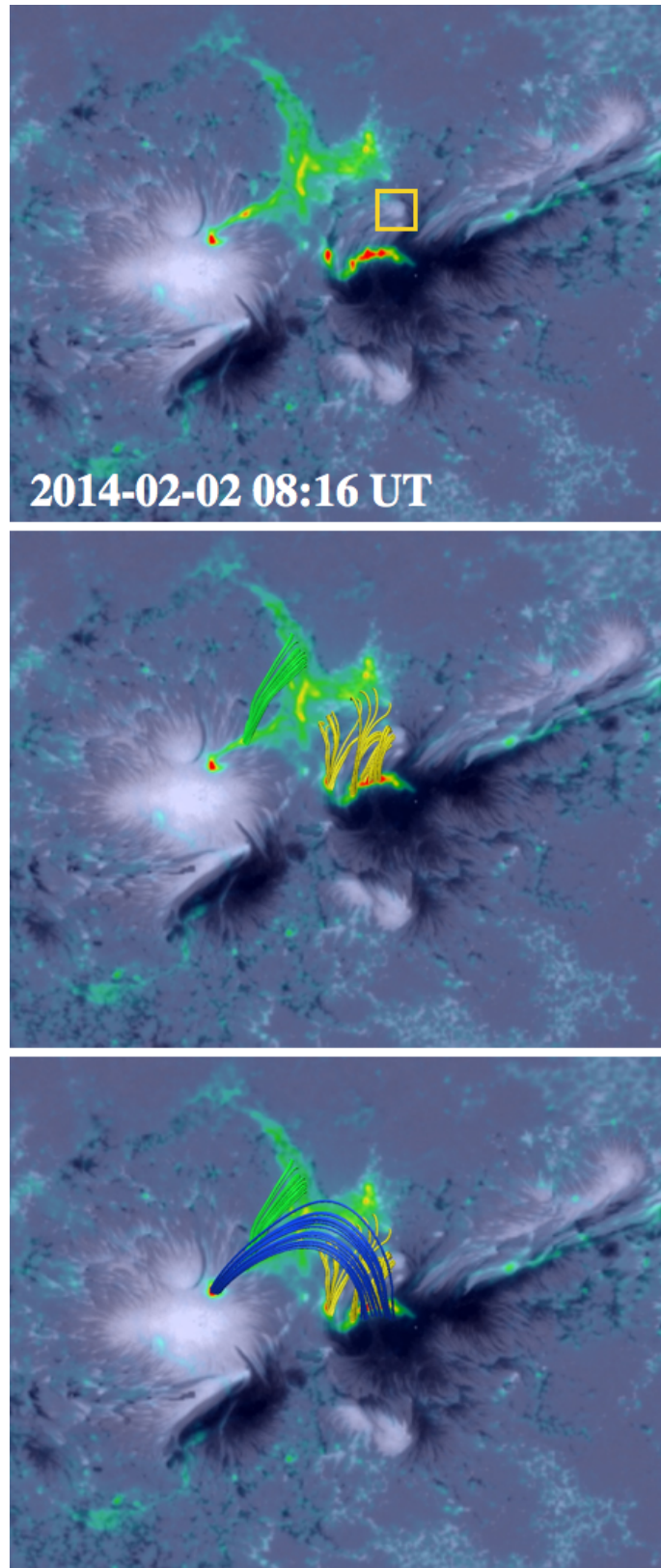


Figure 4.15: The relations of the connectivity of the field lines and the location of flare ribbons in flare 1. The location of flare ribbons observed in AIA 1600 Å are shown by color contours. Yellow field lines from the region of flare ribbons are rooted to the non-flaring region (yellow box).

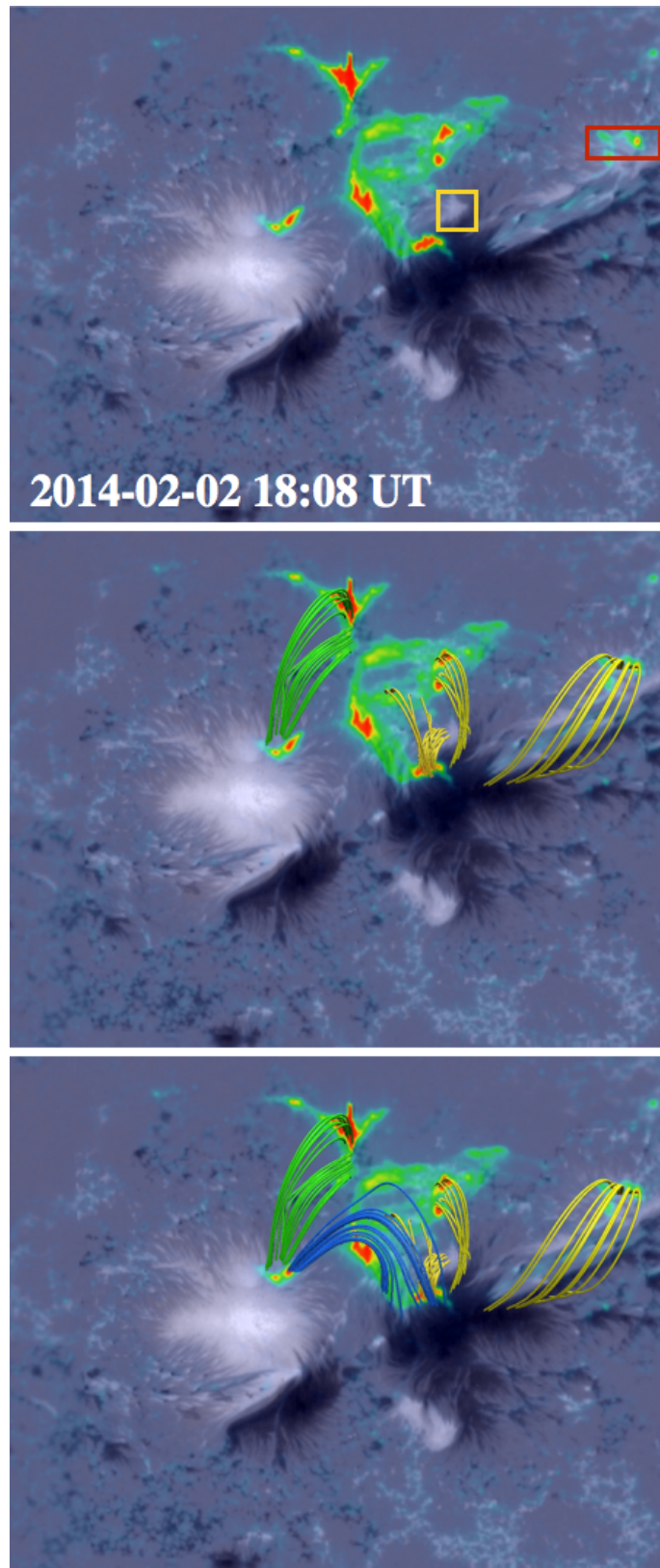
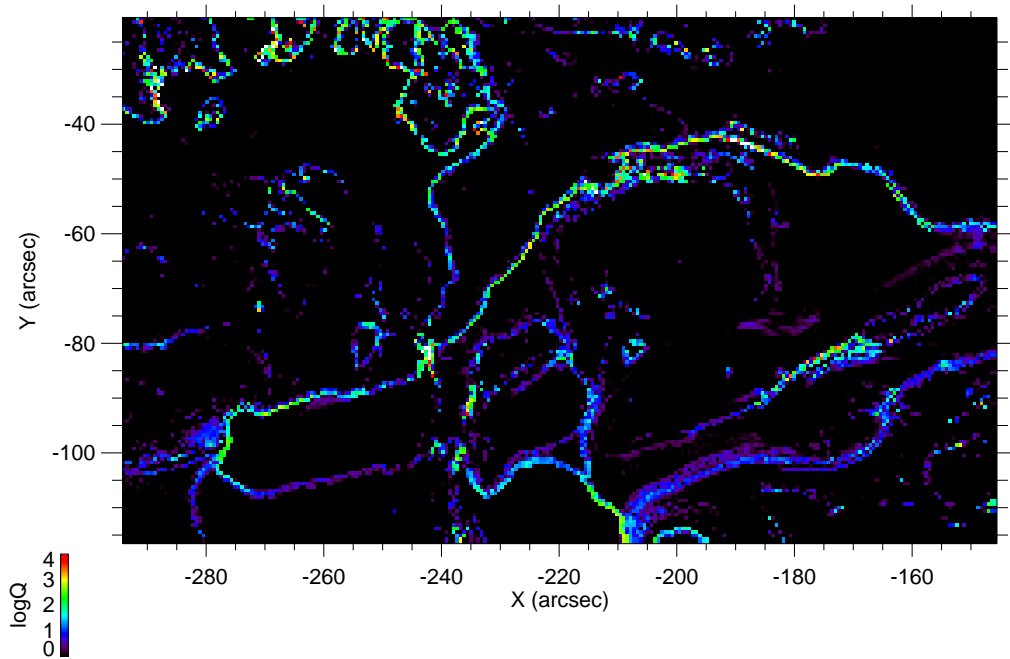
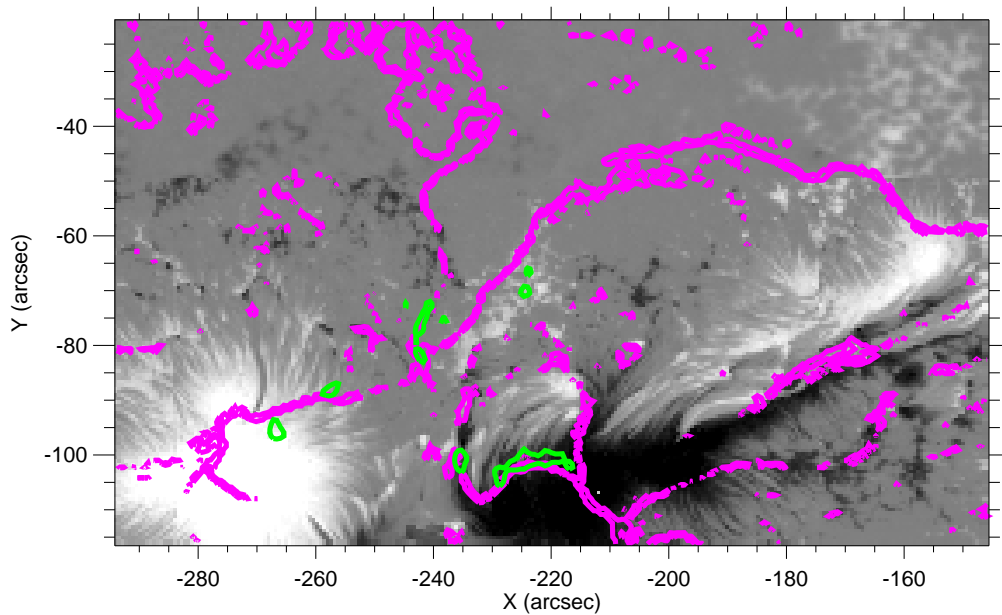


Figure 4.16: Same as Figure 4.15, but in flare 3. Yellow field lines from the region of flare ribbons are rooted to the non-flaring region (to yellow box and from red box).



(a)



(b)

Figure 4.17: (a) The map of the squashing factor at the height about 800 km above the formation layer of the Fe I lines. (b) The vertical component of magnetic field used for the boundary condition of NLFFF modeling. High  $\log Q (> 1)$  are drawn by the purple contour. (a) and (b) is shown by the same field of view.

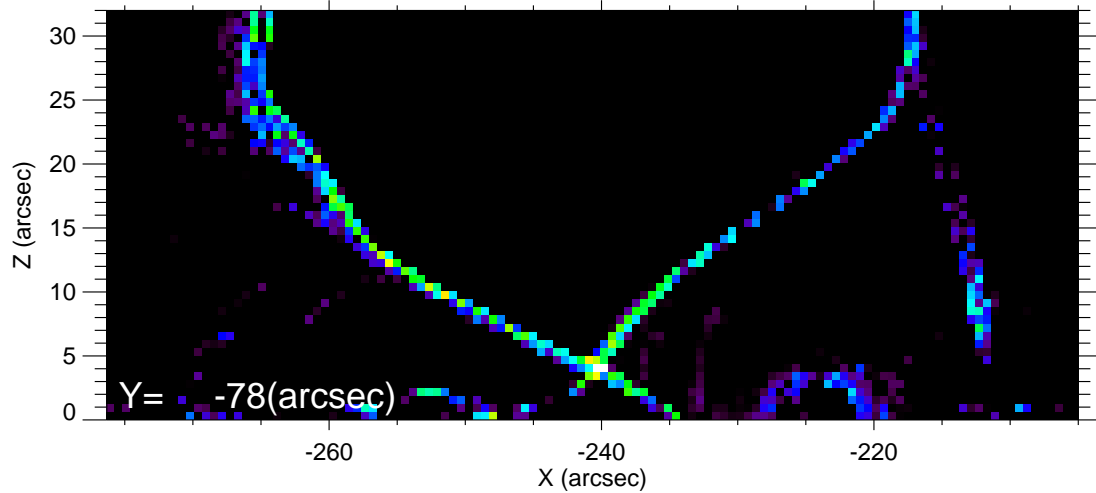


Figure 4.18: The squashing factor in the X-Z plane. The map is in the plane  $y \approx -78$  arcsec in the upper panel of Figure 4.17. There is a region holding the highest squashing factor, where two QSLs are crossing. The height is  $2000 \sim 3000$  km, which correspond to the upper chromosphere or the lower corona.

the plane  $y \approx -78$  arcsec. In this Figure, we can identify a crossing QSLs structure and the intersection has the highest squashing factor in this field of view. The upper sector above the high squashing factor lines are occupied by the magnetic flux labeled P1-N1. The sector at the left of the intersection is the magnetic flux labeled P1-N2, whereas the sector at the right is P2-N1. This shows that the magnetic reconnection most likely occurs at this location. This point is located at the height of  $2000 \sim 3000$  km. The height of  $2000 \sim 3000$  km corresponds to the height of the transition from the chromosphere to the corona in the models of the static atmosphere.

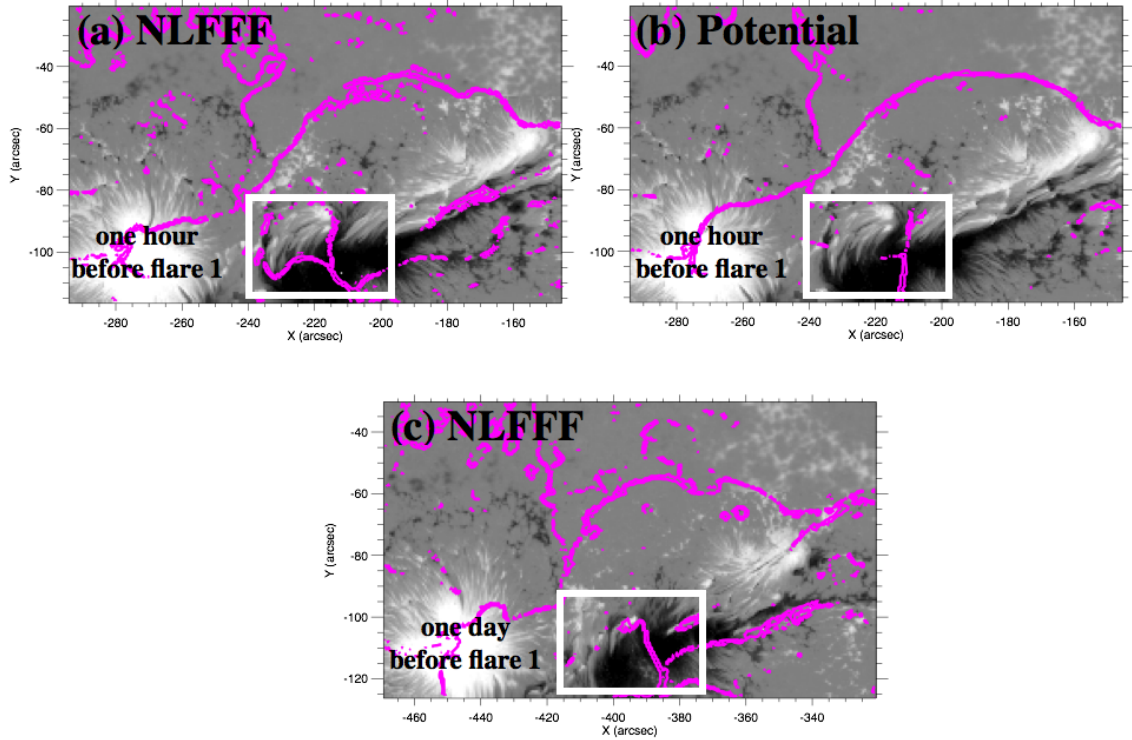


Figure 4.19: (a) The QSLs distribution calculated from the NLFFF one hour before flare 1. (b) The QSLs distribution calculated from the potential field one hour before flare 1. (c) The QSLs distribution calculated from the NLFFF one day before flare 1

### 4.3.2 Formation of the non-potential structure

In Figure 4.19 (a) and (b), we show the QSLs distribution calculated from the NLFFF and the potential field, respectively. The observed time of the magnetic field is same as Figure 4.17. There is a clear difference in the spatial structure of the QSLs in the white box. This indicates that in the region, the magnetic field structure is highly non-potential.

In Figure 4.19 (c), we show the QSLs distribution at one day before flare 1 (between 10:42 and 11:37 on 1 February 2014). In the white box of the bottom panel, we cannot find the QSLs structure as seen in Figure 4.19 (a), which suggest that the QSLs structure in Figure 4.19 (a) was constructed during the day.



# Chapter 5

## Discussion

In this chapter, we discuss our results. There are three points of interest. First, can the NLFFF modeling reconstruct realistic coronal magnetic fields for flares occurring with the quadrupole magnetic field configuration? If not, how can we improve the modeling? Second, we focus on the energy release site and the energy storage in the flaring region. The third interest is the homology and difference in the three flares.

### 5.1 Validity of the NLFFF modeling

As shown in Figure 4.15 and 4.16, the footpoints of the P1-N1 (blue) and P1-N2 (green) magnetic field lines are well co-spatial with flare kernels appeared in the P1, N1, and N2 regions, indicating that the NLFFF modeling successfully reproduces the footpoint connectivity of the coronal magnetic fields involved in the energy release of the flares. Some of the bright kernels in the N1 region also have a good connection to some bright kernels in the P2 region. However, the brightest kernel appeared in the N1 spot region is connected to the nearby positive compact island marked by the yellow box in Figure 4.15 and Figure 4.16, which does not show any flare bright footpoints. There are two possible causes of it. One is that the magnetic fields from the NLFFF modeling are not matched to the actual magnetic field structure because of the plasma condition where the field lines exist. The height at the top of the yellow field lines rooted into the positive island in the

yellow box is only about 1500 km, which may be still below the bottom of the corona. The plasma  $\beta$  in this region may not be sufficiently small according to Figure 1.5, and thus the magnetic field lines from the magnetic island in the yellow box may not be in the force-free state. The other possibility is the magnetic field lines from the yellow box are not involved in the energy release in the flares. Other field lines (P1-N1 and P2-N1) are connected to the region around the bright flare kernels in the N1 sunspot. Thus the flare kernels appeared in the N1 region might be produced by the magnetic reconnection between the P1-N1 and P2-N1 field lines and they are not linked to the field lines from the yellow box. In Figure 4.16, another bright flare footpoint was observed apart from the flaring region at the west edge of the frames. The magnetic field lines from this region marked by the red box are also rooted into a non-flaring region in the negative N1 region. These field lines may correspond to a bright coronal structure seen at the west side of the flare region in Figure 4.9. In our NLFFF modeling, we used the MHD relaxation method with the potential field as an initial condition. The calculation starting from the potential field may reach another force-free field solution when the actual magnetic field structure is significantly derived from the potential field. Such a solution is not matched to the actual magnetic field structure.

For better understanding of solar flares, it is important to know the magnetic field structures formed in the corona where the energy release takes place as precisely as possible and thus we need to improve the fidelity of magnetic field lines with the NLFFF modeling. There are some ideas for improving our NLFFF modeling. One is to use the magnetic field data measured at the chromospheric level, where plasma  $\beta$  is sufficiently small. Our current NLFFF modeling uses the magnetic field data measured at the photospheric level, where the magnetic fields are dominantly controlled by gas dynamics and the magnetic fields may not be in force-free condition. Adding the observational restriction would make the NLFFF modeling more feasible for reconstructing the coronal magnetic field structures. Another idea is to extensively use coronal morphological features seen in EUV and soft X-ray coronal images. Aschwanden et al. (2013) proposed the so-

lution of nonlinear force-free fields with the combination of the photospheric line-of sight magnetograms and coronal loop structures in EUV images. The loop structures seen in EUV images represent the coronal magnetic field lines because the coronal magnetic field is "frozen" in the coronal plasma. Loop-like features seen in EUV images, although they are observed in the 2D, should be used for deriving the force-free magnetic fields more accurately. As our future works, we will acquire the He I 10830 spectra-polarimetric data for deriving magnetic field information at the upper chromosphere at the GREGOR telescope. Deriving the chromospheric magnetic fields with the He I 10830 lines need more works not only in theory but also in observations. These efforts will provide our new methodology with the NLFFF modeling with the combination of the spectra-polarimetric observations for photospheric and chromospheric magnetic fields.

## **5.2 Energy release site and energy storage**

From the location of the flare ribbons and the photospheric magnetic field distribution, we found that four magnetic polarities (P1, P2, N1, and N2) contributed to the flares shown in Figure 4.4. The NLFFF modeling provided the three-dimensional coronal magnetic field structures shown in Figure 4.12. There exist four magnetic flux domains (P1-N1, P1-N2, P2-N1, and P2-N2) and a null like structure in the center of the four domains. Figure 4.17 (b) gives the location of the bright flare kernels in flare ribbons in flare 1 on the vertical magnetic flux distribution, which are compared with the chromospheric location of QSLs. Most of the bright flare kernels are located on or very close to the chromospheric location of QSLs. In flare 1, the flare kernels on the sunspots (P1 and N1) are located on the position of the QSLs with the accuracy of less than a few arcsec. The flare kernels in the plage region P2 are located slightly apart from the QSL, as illustrated in Figure 5.1. Although we did not show the data in chapter 4, the same relation between the flare ribbons and the QSLs can be seen in flare 3. This means that the magnetic field P2-N2 did not contribute to the energy release of the flares, and the QSLs on the

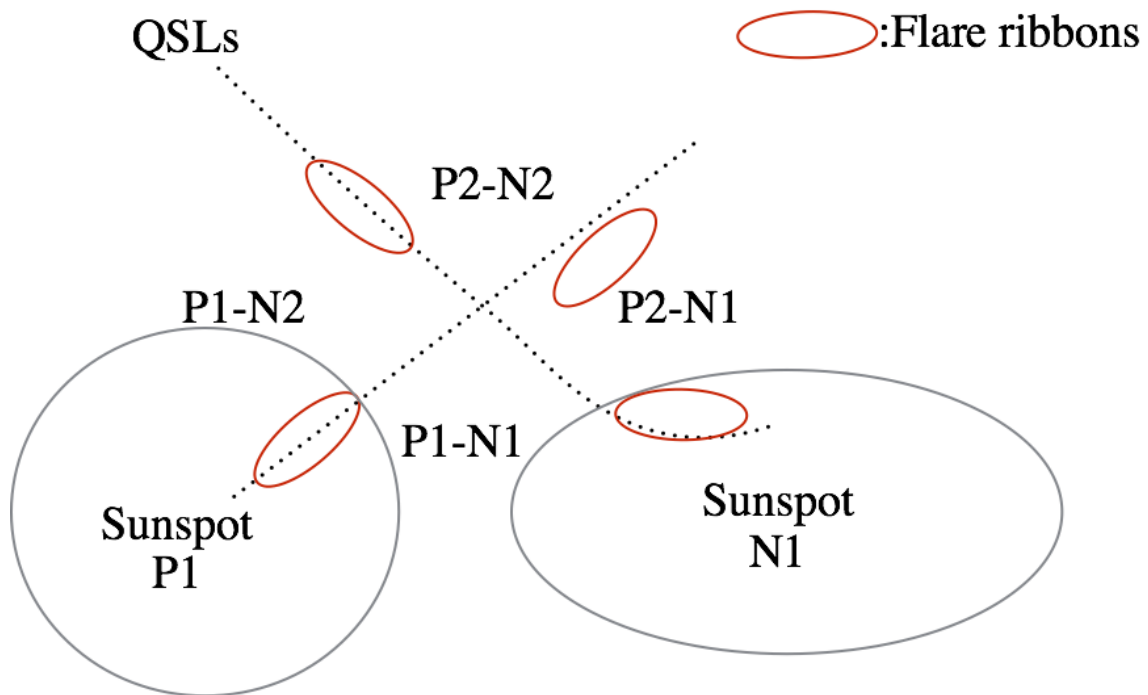


Figure 5.1: The sketch describing the relation between flare ribbons and QSLs. Red lines show the location of the flare ribbons. Black dotted lines give the position of the QSLs at the chromospheric level. Flare ribbons are located on or close to the QSLs, which separate the magnetic flux into four flux domains, namely P1-N1, P2-N1, P1-N2 and P2-N2.

sunspots are more important for the occurrence of these flares. The overview of the three-dimensional magnetic fields, viewed from the two different directions, is illustrated in Figure 5.2. A blue solid line, yellow, and green dashed lines show the P1-N1, P2-N1, and P1-N2 magnetic field lines, respectively. Figure 5.2 (a) and (b) show the magnetic field structure viewed from +z direction and +x direction, respectively. From Figure 4.18, the highest Q factor exists at 2000~3000km height and shows a null point like structure. Our results indicate that the magnetic reconnection can occur around this site, which is located at relatively lower atmosphere.

The magnetic field lines P1-N1 is highly inclined and covers the site of the main energy release, as illustrated in Figure 5.2 (b). As shown in Figure 4.19, the magnetic field on the N1 has highly non-potential structure. The candidate which generated the structure is thought to be the emergence of magnetic flux or the transverse photospheric motion. We can identify both candidates as shown in Figure 4.5 and Figure 4.6. Conversely motion of

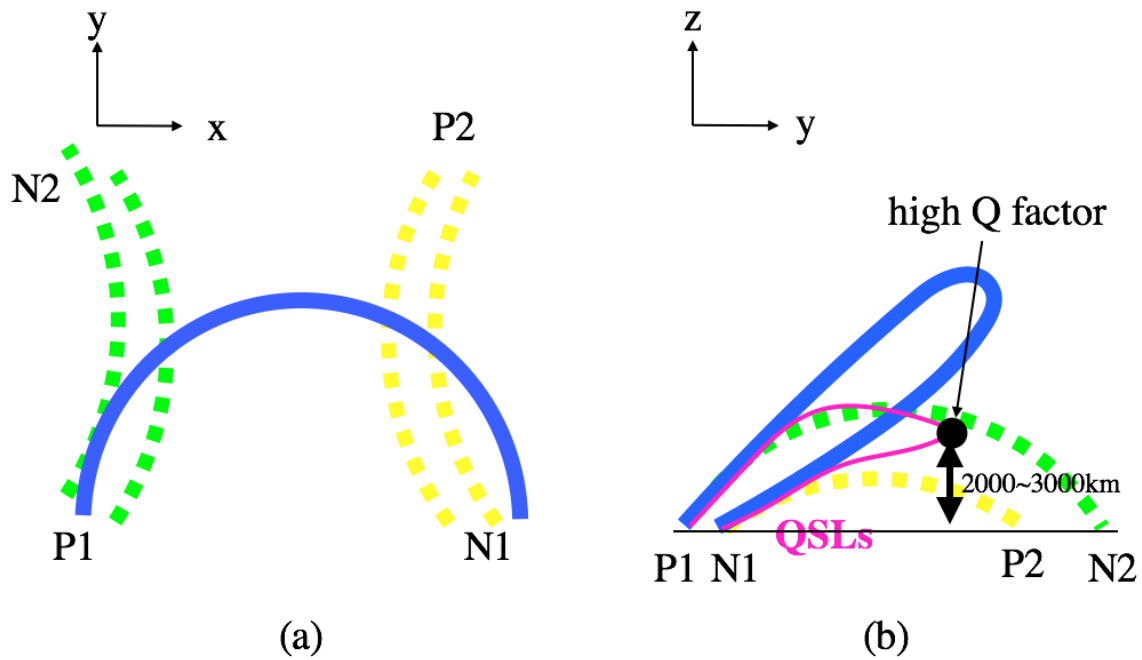


Figure 5.2: Magnetic structures with the P1-N1, P1-N2, and P2-N1 magnetic fields, viewed from the two directions. The site of the main energy release may be located at the height of 2000~3000 km above the solar structure, which is covered by the P1-N1 magnetic flux.

two sunspots and emerging flux in N1 region were found near the flaring region. Figure 4.6 showed the increase of magnetic flux in the N1 region, i.e., the emergence of magnetic flux. This results indicate that the non-potential structure was generated by the emergence of magnetic flux.

### 5.3 Homology and differences in the flares

Using the Hinode SP and SDO observations, we studied three flares that occurred at the same region within 12 hours on 2 February 2014. Homology and difference in the three flares were described in chapter 4. They showed bright coronal structures similar to each other as well as chromospheric flare ribbons similar to each other. Homology in the bright structure and chromospheric flare ribbons indicates the similar coronal magnetic structures and the similar energy release site. The soft X-ray flux plots, however, showed that the temporal profile of flare 2 and 3 is different from that of flare 1. We suspect that

this difference may attribute to the different preflare activities as shown in Figure 4.10 and 4.11. In flare 1, another flare started at about one hour before the onset of flare 1 at the east of the flare 1 location, as shown in Figure 4.10. The magnetic field relating to this flare forms a large-scale structure overlying the site of flare 1, as shown in Figure 4.13. After the occurrence of the previous flare, the magnetic tension from the overlying magnetic structures may decrease, that might result in disturbing the lower magnetic field structure, which is similar to the case of the breakout model (Antiochos et al., 1999). On the other hand, the ejecting dark material was observed before flare 2 (Figure 4.11). The upward motion of the dark material might lift up the overlying coronal magnetic structure and reduce the magnetic tension, leading to flare 2. Our results by EUV observations and NLFFF modeling suggest that the difference in preflare activities can lead to the difference in the X-ray flux light curve. Note that there was no ejection and other flare activities observed around flare 3.

## **5.4 Comparison with the previous studies and outlooks**

There are two new points in our study. First, we investigated temporal variation of three-dimensional quadrupole magnetic fields. Chandra et al. (2011) investigated quadrupole three-dimensional magnetic field just before a few minutes of the flare occurrence. Our study shows the evolution of QSLs (Figure 4.19) in one day and suggests that the creation of non-potential QSLs might contribute to flare 1. In this thesis, we do not discuss the QSLs after flare 1. It is difficult to discuss the cause of flare 2 and flare 3, since the photospheric magnetic fields show little change before and after the flare occurrence (especially between flare 1 and flare 2). So the extrapolated magnetic fields also tend to be similar to each other. In order to understand the repetition of flares, we need another boundary condition, such as the magnetic field in the chromosphere. Second, Our study also show the magnetic reconnection site in the low atmosphere (2000~3000km). Although Schmieder et al. (2007) also discuss the height of the null point, they only discuss the null

point above 10 Mm. This is because they use the low spatial resolution and they could not resolve the magnetic structure in the low atmosphere. The high spatial resolution of *Hinode/SP* enables us to extrapolate the high spatial three-dimensional magnetic structure and discuss the detailed magnetic structure in the lower atmosphere. In order to confirm the importance of the magnetic structure in the low atmosphere for the occurrence of solar flares, we need to investigate the three-dimensional structure statistically.



# Chapter 6

## Summary and Future Works

With observations carried by *Hinode* and *SDO* satellites, we investigate three M-class (M2.2, M4.4, and M3.1) flares occurring on 2 February 2014. They are called, flare 1, flare 2, and flare 3 in these thesis. Our investigations primarily focused on the 3D coronal magnetic field structures formed in the flaring region for attempting to understand why three similar flares are successively produced in the region. The following three topics are mainly discussed in this thesis; 1) how well the coronal magnetic structure is inferred with a NLFFF modeling in the region where the flares are produced?; 2) what is 3D magnetic field configuration and where is the site of the main energy release located in the 3D magnetic configuration? and 3) what is the homology and difference seen in these three flares?

UV and EUV observations by AIA aboard the *SDO* suggested the complex magnetic structures in the corona. Four flare ribbons appeared in AIA chromospheric 1600 Å images, and three flaring structure in AIA coronal 131 Å images. These flares showed quite similar flare ribbons and flaring coronal structures. Because of these features, they can be called homologous flares. The flare ribbons were located at the quadrupole distribution of four magnetic regions (P1, P2, N1, and N2). Although the spatial distribution of the flare ribbons in the later stage of the flares is similar to each other in the main period of the flares, there is a little difference in the temporal evolution of X-ray flux. While flare 1 has

the temporal profile of X-ray flux with two different phases (a gradual increase and a rapid increase to the peak flux), flare 2 and flare 3 have only one rapid increase in the X-ray flux. Such a difference might attribute to the difference in triggering the onset of these flares. Focused on flare 1 and flare 2, flare 1 occurred after the occurrence of another flare event at the east side of the flare 1 region, while flare 2 occurred after the upward motion of a dark material. This may indicate that the magnetic field shows a similar topology, but the trigger mechanism can alter the temporal behaviors of the energy release.

We derived the three dimensional magnetic field configuration at the site of the flares using the force-free field modeling developed by Inoue et al. (2014). The vector magnetic field data obtained by the SP on board the *Hinode* spacecraft with the complementary HMI data are used for the boundary condition on the solar surface. The results of the force-free field modeling show the good agreement with the connectivity of the footpoints magnetic field lines identified for many bright flare kernels. The results, however, provided a couple of examples in poor connection of magnetic field lines to flare kernels. This indicates that we still need to pay careful attentions to the results from the NLFFF modeling, although the magnetic field lines showing a good match with the location of flare kernels can be used in the further analysis.

We used the squashing factor defined by Titov (1999) to identify the location of quasi-separatrix layers, i.e., QSLs. We investigated the location holding the highest squashing factor, where the magnetic reconnection is most likely to occur. The region of the highest value is located at the height of 2000~3000km from the photosphere, which corresponds to the height between the upper chromosphere and the lower corona. This suggests that the magnetic reconnection may take place at the lower atmosphere. The magnetic flux in the N1 sunspot appears to be highly twisted, because the QSLs structure derived with the assumption of the potential field is completely different from what obtained with 3D magnetic field configuration from the NLFFF modeling. Furthermore, the QSLs structure derived with the NLFFF results for the SP data taken one day before the occurrence of flare 1 is different from that derived with the data taken one hour before flare 1. This

indicates that the QSLs structure was formed during the day due to the emergence or the transverse photospheric motions of the magnetic flux in N1. The temporal evolution of magnetic flux suggests that both the existence of emerging activities and the converging motions in and around the N1 sunspot region.

From our results, we recognize some important issues which should be addressed in future works. One is the improvement of the NLFFF modeling for deriving the 3D magnetic field structures in the corona. As discussed in chapter 5, one solution is to include the information from chromospheric field measurements in the NLFFF modeling. Measurements of chromospheric magnetic fields are challenging efforts, but some progresses have been taken with the ground-based telescopes, such as Tenerife Infrared Polarimeter (TIP) equipped to the Vacuum Tower Telescope (VTT) in Tenerife. Yelles Chaouche et al. (2012) performed a force-free field modeling using both photospheric and chromospheric magnetic fields (Si I 10827 Å and He I 10830 Å) independently. By using the He I 10830 Å line, chromospheric magnetic fields from tens of Gauss to kilo Gauss can be measured with the Hanle effect and the Zeeman effect (Trujillo Bueno et al., 2002; Trujillo Bueno & Asensio Ramos, 2007). They used only the Zeeman effect and concluded that by using magnetic fields at multi layers and comparing with each other, the solution of 180 degree ambiguity is improved. Their work focused on the active region filament. Their data is low spatial resolution (1'') and limited field of view ( $\sim 30'' \times 30''$ ). A new large-aperture telescope called GREGOR recently started its operations, providing the Stokes polarimetric data with the spatial resolution higher than that of the TIP. We are currently planing to observe an active region with a wide field of view. When we acquire the data coordinated with *Hinode* and *SDO/AIA*, we will investigate how the magnetic fields can be derived at the chromosphere with the combination of the Zeeman and Hanle effects. We will also investigate improvements on force-free field modeling with adding the chromospheric magnetic field.

The second challenge is to understand the temporal evolution of magnetic structures and its association with flare triggering. For such studies, we need to carry out the 3D

MHD simulation based on observations. Since the force-free field is in equilibrium state, we cannot investigate the temporal dynamics only with deriving a snapshot of the 3D magnetic field structure by force-free field modeling. We will consider to use the force-free field derived from observations as an initial condition and solve MHD equations by evolving the bottom boundary condition with observed magnetic field in the photosphere. The concept is similar to Inoue et al. (2014). While they used potential the field as an initial condition to obtain a force-free state, we will use the NLFFF at one observed time and change the bottom boundary condition gradually based on the information from the temporal evolution of observed magnetic fields in the photosphere. In the first step, we solve zero  $\beta$  single fluid MHD equations, and then plan to add the physical effects such as gravity, gas pressure (non zero  $\beta$ ), and weakly ionized plasma (multi fluid). Adding such effects, we can describe magnetic fields existing in the lower atmosphere more correctly.



# Acknowledgments

I would like to show my greatest appreciation to my supervisor, Dr. Toshifumi Shimizu for his insightful comments and suggestions throughout the course of my study. I would also like to express my gratitude to Dr. Satoshi Inoue for helpful discussions as a collaborator. I have had the support and encouragement of all the members in my laboratory, T., Sakao, D., Brooks, T., Matsumoto, Lee Kyoung-Sun, Carlos Quite Noda, Y., Iida, S., Ishikawa, M., Ohyama, Y., Bamba, T., Oba, R., Kanoh, M., Yamada, T., Okamoto, K., Watanabe, K., Daiguji. Numerical computations were carried out on Supercomputer for earth Observation, Rockets, and Aeronautics (SORA) of Japan Aerospace Exploration Agency, JAXA. I am also grateful to my family for their warm and hearty support.



# References

- Antiochos, S. K., DeVore, C. R., & Klimchuk, J. A. 1999, *ApJ*, 510, 485
- Aschwanden, M. J., Boerner, P., & AIA/SDO Team. 2013, in *AAS/Solar Physics Division Meeting*, Vol. 44, *AAS/Solar Physics Division Meeting*
- Aulanier, G. 2014, in *IAU Symposium*, Vol. 300, *IAU Symposium*, ed. B. Schmieder, J.-M. Malherbe, & S. T. Wu, 184–196
- Aulanier, G., DeLuca, E. E., Antiochos, S. K., McMullen, R. A., & Golub, L. 2000, *ApJ*, 540, 1126
- Aulanier, G., Török, T., Démoulin, P., & DeLuca, E. E. 2010, *ApJ*, 708, 314
- Aulanier, G., et al. 2007, *Science*, 318, 1588
- Bateman, G. 1978, *MHD instabilities*
- Bobra, M. G., Sun, X., Hoeksema, J. T., Turmon, M., Liu, Y., Hayashi, K., Barnes, G., & Leka, K. D. 2014, *Sol. Phys.*, 289, 3549
- Brandt, A. 1977, *Mathematics of computation*, 31, 333
- Carmichael, H. 1964, *NASA Special Publication*, 50, 451
- Chandra, R., Schmieder, B., Mandrini, C. H., Démoulin, P., Pariat, E., Török, T., & Uddin, W. 2011, *Sol. Phys.*, 269, 83
- Chen, P. F., & Shibata, K. 2000, *ApJ*, 545, 524

- Dalmasse, K., Chandra, R., Schmieder, B., & Aulanier, G. 2015, *A&A*, 574, A37
- Dedner, A., Kemm, F., Kröner, D., Munz, C.-D., Schnitzer, T., & Wesenberg, M. 2002, *Journal of Computational Physics*, 175, 645
- del Toro Iniesta, J. C. 2007, *Introduction to Spectropolarimetry*
- Demoulin, P., Henoux, J. C., Priest, E. R., & Mandrini, C. H. 1996, *A&A*, 308, 643
- Dudík, J., Janvier, M., Aulanier, G., Del Zanna, G., Karlický, M., Mason, H. E., & Schmieder, B. 2014, *ApJ*, 784, 144
- Dungey, J. 1953, *The London, Edinburgh, and Dublin Philosophical Magazine and Journal of Science*, 44, 725
- Emonet, T., & Moreno-Insertis, F. 1998, *ApJ*, 492, 804
- Forbes, T. G., & Priest, E. R. 1984, *Sol. Phys.*, 94, 315
- Gaizauskas, V. 1982, *Advances in Space Research*, 2, 11
- Gaizauskas, V., & Svestka, Z. 1987, *Sol. Phys.*, 114, 389
- Gary, G. A. 2001, *Sol. Phys.*, 203, 71
- Hara, H., Watanabe, T., Harra, L. K., Culhane, J. L., & Young, P. R. 2011, *ApJ*, 741, 107
- Heyvaerts, J., Priest, E., & Rust, D. M. 1977, *Sol. Phys.*, 53, 255
- Hirayama, T. 1974, *Sol. Phys.*, 34, 323
- Ichimoto, K., et al. 2008, *Sol. Phys.*, 249, 233
- Inoue, S., Magara, T., Pandey, V. S., Shiota, D., Kusano, K., Choe, G. S., & Kim, K. S. 2014, *ApJ*, 780, 101
- Janvier, M., Aulanier, G., & Démoulin, P. 2015, *Sol. Phys.*

- Janvier, M., Aulanier, G., Pariat, E., & Démoulin, P. 2013, *A&A*, 555, A77
- Kliem, B., & Török, T. 2006, *Physical Review Letters*, 96, 255002
- Kopp, R. A., & Pneuman, G. W. 1976, *Sol. Phys.*, 50, 85
- Kosugi, T., et al. 2007, *Sol. Phys.*, 243, 3
- Kusano, K., Bamba, Y., Yamamoto, T. T., Iida, Y., Toriumi, S., & Asai, A. 2012, *ApJ*, 760, 31
- Leka, K. D., Canfield, R. C., McClymont, A. N., & van Driel-Gesztelyi, L. 1996, *ApJ*, 462, 547
- Lemen, J. R., et al. 2012, *Sol. Phys.*, 275, 17
- Lites, B. W., & Ichimoto, K. 2013, *Sol. Phys.*, 283, 601
- Lites, B. W., Low, B. C., Martinez Pillet, V., Seagraves, P., Skumanich, A., Frank, Z. A., Shine, R. A., & Tsuneta, S. 1995, *ApJ*, 446, 877
- Lites, B. W., Martinez Pillet, V., & Skumanich, A. 1994, *Sol. Phys.*, 155, 1
- Liu, R., Titov, V. S., Gou, T., Wang, Y., Liu, K., & Wang, H. 2014, *ApJ*, 790, 8
- Louis, R. E., Puschmann, K. G., Kliem, B., Balthasar, H., & Denker, C. 2014, *A&A*, 562, A110
- Martres, M.-J., Mouradian, Z., & Soru-Escout, I. 1984, *Advances in Space Research*, 4, 31
- McKenzie, D. E., & Canfield, R. C. 2008, *A&A*, 481, L65
- Mikic, Z., & McClymont, A. N. 1994, in *Astronomical Society of the Pacific Conference Series*, Vol. 68, *Solar Active Region Evolution: Comparing Models with Observations*, ed. K. S. Balasubramaniam & G. W. Simon, 225

- Morita, S., Uchida, Y., Hirose, S., Uemura, S., & Yamaguchi, T. 2001, *Sol. Phys.*, 200, 137
- Nagashima, K., & Yokoyama, T. 2006, *ApJ*, 647, 654
- Panesar, N. K., Sterling, A. C., Innes, D. E., & Moore, R. L. 2015, *ApJ*, 811, 5
- Pariat, E., & Démoulin, P. 2012, *A&A*, 541, A78
- Parker, E. N. 1963, *ApJS*, 8, 177
- Pesnell, W. D., Thompson, B. J., & Chamberlin, P. C. 2012, *Sol. Phys.*, 275, 3
- Petschek, H. E. 1964, *NASA Special Publication*, 50, 425
- Priest, E. 2014, *Magnetohydrodynamics of the Sun*
- Priest, E. R., & Démoulin, P. 1995, *J. Geophys. Res.*, 100, 23443
- Rachkovsky, D. N. 1962, *Izvestiya Ordena Trudovogo Krasnogo Znameni Krymskoj Astrofizicheskoj Observatorii*, 28, 259
- Schindler, K., Hesse, M., & Birn, J. 1988, *J. Geophys. Res.*, 93, 5547
- Schmidt, H. U. 1964, *NASA Special Publication*, 50, 107
- Schmieder, B., Mandrini, C. H., Démoulin, P., Aulanier, G., Li, H., & Berlicki, A. 2007, *Advances in Space Research*, 39, 1840
- Schou, J., et al. 2012, *Sol. Phys.*, 275, 229
- Shimizu, T., et al. 2008, *Sol. Phys.*, 249, 221
- Socas-Navarro, H. 2001, in *Astronomical Society of the Pacific Conference Series*, Vol. 236, *Advanced Solar Polarimetry – Theory, Observation, and Instrumentation*, ed. M. Sigwarth, 487

- Sturrock, P. A. 1966, *Nature*, 211, 697
- Suematsu, Y., et al. 2008, *Sol. Phys.*, 249, 197
- Sweet, P. A. 1958, in *IAU Symposium, Vol. 6, Electromagnetic Phenomena in Cosmical Physics*, ed. B. Lehnert, 123
- Titov, V. 1999, in *ESA Special Publication, Vol. 448, Magnetic Fields and Solar Processes*, ed. A. Wilson & et al., 715
- Titov, V. S. 2007, *ApJ*, 660, 863
- Titov, V. S., Hornig, G., & Démoulin, P. 2002, *Journal of Geophysical Research (Space Physics)*, 107, 1164
- Trujillo Bueno, J., & Asensio Ramos, A. 2007, *ApJ*, 655, 642
- Trujillo Bueno, J., Landi Degl’Innocenti, E., Collados, M., Merenda, L., & Manso Sainz, R. 2002, *Nature*, 415, 403
- Tsuneta, S. 1996, *ApJ*, 456, 840
- Tsuneta, S., et al. 2008, *ApJ*, 688, 1374
- Unno, W. 1956, *PASJ*, 8, 108
- Wiegelmann, T., & Sakurai, T. 2012, *Living Reviews in Solar Physics*, 9, 5
- Yelles Chaouche, L., Kuckein, C., Martínez Pillet, V., & Moreno-Insertis, F. 2012, *ApJ*, 748, 23